

## Effect of specific surface area on the rheological properties of graphene nanoplatelet/poly(ethylene oxide) composites

Haritha Haridas, Marianna Kontopoulou\*

Department of Chemical Engineering, Graphene Integrated Functional Technologies, Dupuis Hall, Queen's University, 19 Division Street, Kingston, ON K7L 3N6, Canada

### Synopsis

The rheological properties of poly(ethylene oxide) containing graphene nanoplatelets (GNPs) having different specific surface areas (SSAs) are studied using steady shear and small amplitude oscillatory shear experiments. A series of GNPs having SSAs ranging from  $175 \pm 5$  to  $430 \pm 13$  m<sup>2</sup>/g was prepared using a thermomechanical exfoliation process. The complex viscosity, moduli and yield stress of the composites increase with SSA, whereas the electrical and rheological percolation threshold concentrations decrease, suggesting that higher SSAs promote filler network formation. Modeling of the small amplitude oscillatory shear data using a two-phase model confirms that hydrodynamic effects dominate at low concentrations below 8 wt.%, where the particles are non-interacting. At higher concentrations the response is dominated by the filler-phase contributions. We demonstrate that the two-phase model parameters can be used to track the exfoliation of graphite into GNPs. Fitting of the rheological percolation curves using the Utracki and Lyngaae-Jørgensen models at low concentrations (non-interacting regime) resulted in aspect ratios between 19-76. At high concentrations (interacting particles) the aspect ratios determined by the Krieger-Daugherty model ranged between 5-24, due to aggregation. The highest aspect ratios (defined as ratio of major dimension to minor dimension) were associated with GNPs that had the highest SSA of 430 m<sup>2</sup>/g. Strain sweeps revealed that the critical strain for the onset of non-linear viscoelasticity scaled with SSA above the percolation threshold. The scaling relationships of the critical strain and storage modulus with volume fraction were used to infer the fractal dimensions of the filler networks.

\*Corresponding author: Marianna Kontopoulou (kontopm@queensu.ca)

## I. INTRODUCTION

Carbonaceous nanoparticles such as carbon nanotubes (CNTs), graphene, and graphene nanoplatelets (GNPs) have gained significant interest through the last decade, due to their superior properties and multiple functionalities. Large surface areas, high aspect ratios, along with high modulus, and inherent thermal and electrical conductivity make these materials forerunners as additives in polymer composites, and as components in formulations of conductive inks, anticorrosion coatings, supercapacitors, heat spreaders, and in electronics and photonics applications [Zhu *et al.* (2018)]. Specifically, the demand for high quality, defect-free, few- and multi-layered (FLG and MLG respectively) GNPs has risen over the recent years due to their lower costs and ease of production compared to CNTs [King *et al.* (2011), Su *et al.* (2021), Yang *et al.* (2012)]. GNPs can be manufactured in large quantities using top-down approaches [Zhu *et al.* (2018)], which are suitable for large volume applications [Zurutuza and Marinelli (2014)]. There are several top-down methods in which GNPs are derived from graphite, which has a sheet-like structure. The graphite layers have strong bonding between the atoms on a hexagonal plane, but weak bonding in the normal plane, and therefore they can be delaminated to produce few- and multi-layered GNPs [Mardlin *et al.* (2022a), Yasmin *et al.* (2006)].

GNPs manufactured using top-down approaches generally have a broad particle size and thickness distribution and contain fractions of unexfoliated micro-graphite particles in the final product [Lin *et al.* (2019), Zurutuza and Marinelli (2014)] causing large discrepancies in the quality and performance [Kong *et al.* (2019), Lin *et al.* (2019), Ye and Tour (2019)]. Hence, there is a need for rigorous and convenient characterization techniques that can adequately describe the properties of the GNPs, and determine their suitability in various applications [Kong *et al.* (2019), Lin *et al.* (2019), Ren and Cheng (2014), Ye and Tour (2019)]. The common characterization techniques include Brunauer-Emmett-Teller (BET), X-ray diffraction (XRD), and small angle X-ray scattering (SAXS); imaging techniques such as scanning electron microscopy (SEM), transmission electron microscopy (TEM), and atomic force microscopy (AFM); spectroscopy techniques such as X-ray photoelectron spectroscopy (XPS), and Raman spectroscopy [Aram

*et al.* (2016), Hernandez *et al.* (2008), Ye and Tour (2019), Rahmanian and Galeski (2021), Ferreira *et al.* (2019)]. Some of these techniques such as TEM, AFM and Raman spectroscopy only analyse a small part of the sample and therefore they are not representative of the bulk material [Ghanbari *et al.* (2013), Kong *et al.* (2019)], whereas Raman spectroscopy, XPS and SAXS require specialized equipment and are expensive and time consuming. Recently Buzaglo *et al.* (2017) used a bulk characterization technique, thermogravimetric analysis (TGA), to detect and quantify the conversion of graphite into graphene sheets.

In comparison to other analytical techniques, rheological characterization of dispersions and nanocomposites is fairly simple, reproducible and advantageous as it probes the bulk properties of these materials [Ghanbari *et al.* (2013)]. Small amplitude oscillatory shear (SAOS) characterization has been previously used to quantify levels of exfoliation in layered nanofillers, as well as the level of polymer/filler and filler/filler interactions in nanocomposites [Abdel-Goad *et al.* (2007), Bailly and Kontopoulou (2013), Vergnes (2011), Zohrevand *et al.* (2014)]. Nanofillers generate unique rheological signatures related to their microstructure when dispersed in fluids or when mixed with polymer melts depending on the extent of exfoliation, orientation, and particle-particle interactions [Abdel-Goad *et al.* (2007), Barwich *et al.* (2015), Song and Zheng (2015), Vergnes (2011), Vermant *et al.* (2007)]. Rheology is therefore a very versatile method to supplement the microstructural characterization of nanofillers [Bailly *et al.* (2010), Beuguel *et al.* (2018), Song (2006), Vergnes (2011), Vermant *et al.* (2007), Baeza *et al.* (2016)].

The mesoscale structure and strength of polymer-nanoparticle interactions can also be investigated using viscoelastic measurements [Krishnamoorti and Yurekli (2001), Chen *et al.* (2015), Baeza *et al.* (2016)]. The effect of particle size, shape/aspect ratio, specific surface areas, interface in the dispersion/matrix and level of dispersion on the rheology can be successfully differentiated and quantified with controlled rheological experiments.

The surface area and aspect ratio are the two important geometric features of the nanoparticles that are of particular interest [Akpan *et al.* (2019), Aoyama *et al.* (2020), Joseph *et al.* (2002)]. Typically, rod shaped

particles, followed by platelet shaped fillers, lead to much higher increase in viscosities in comparison to spherical fillers in dispersions [Joseph *et al.* (2002), Nutz *et al.* (1997), Yuan and Murray (1997)]. Increasing the specific SSAs of the fillers has also shown a noteworthy increase in viscosities in both dispersions and melts [Graziano *et al.* (1979), Joseph *et al.* (2002)]. The SSA and aspect ratio directly affect the interfacial area of the fillers in the dispersions and melts, and also determine the level of interaction between the particles [Abdel-Goad *et al.* (2007), Akpan *et al.* (2019)]. A study on the rheology of carbon black dispersions in low molecular weight Newtonian liquids by Graziano *et al.* (1979) showed that the viscosity of these dispersions increased with increasing SSA of the carbon black; the strength of the aggregate network formed at high concentrations due to the filler-filler interactions was dependent on the surface area of the carbon black. The average size of the particles and their size distribution are also important parameters affecting suspension rheology [Barnes (2003), Metzner (1985)]. Chen *et al.* (2015) showed that smaller sized nanoparticles in poly(2-vinylpyridine)/silica nanocomposites led to rheological percolation at lower concentrations and stronger reinforcement arising from glassy polymer bridges between neighbouring nanoparticles, as opposed to rubbery (flexible) bridges for larger sized nanoparticles.

Although the rheological properties of graphene oxide (GO) dispersions have been widely reported, studies on dispersions and composites containing GNPs are relatively scarce. One of the reasons is that GNPs are difficult to disperse within many common solvents and polymer matrices, due to their aggregating nature arising from the  $\pi$ - $\pi$  stacking interactions, and the absence of specific interactions with the solvent or polymer matrix, stemming from the lack of functional groups on the GNP surface [Sabzi *et al.* (2013)]. On the other hand, the absence of surface charges in GNPs makes it easier to interpret their effects on the rheological properties of dispersions and composites [Barwich *et al.* (2015)].

Several studies on the SAOS rheology of GNPs dispersed in organic solvents and polymer matrices have been previously reported [El Achaby *et al.* (2012), Hadaeghnia *et al.* (2020), Li *et al.* (2011), Mayoral *et al.* (2015), Mohamadi *et al.* (2019), Yang *et al.* (2012)]. Barwich *et al.* (2015) demonstrated rheological percolation (defined as the divergence of the zero-shear viscosity and elastic modulus  $G'$ ) at 0.2 vol.% for

GNP dispersions in n-methyl-pyrrolidine. The melt rheology of GNPs dispersed in poly(propylene) (PP) and poly(amide) (PA) 6 matrices was studied by Li *et al.* (2011) and Mayoral *et al.* (2015), with both studies reporting rheological percolation around 15 wt.% (~ 8.5 vol.%) GNP concentrations. The effect of GNP particle size was explored by Beuguel *et al.* (2018) in a PP matrix. Sabzi *et al.* (2013) studied the effect of two types of GNPs, varying in SSA, aspect ratios and oxygen containing surface groups when dispersed in poly(lactic acid). GNPs with the higher SSA, larger aspect ratio and higher oxygen content resulted in the formation of a percolated filler network at a lower concentration (0.39 vol.% as opposed to 4.4 vol.%) and had a stronger filler network in comparison to the other GNPs, due to their good dispersion within the PLA matrix. We note that a wide range of values for the rheological percolation thresholds has been reported in the literature for GNP systems and no consensus has emerged yet. Although typically fillers with higher aspect ratio demonstrate lower rheological percolation thresholds [Aoyama *et al.* (2020)], research by Kalaitzidou *et al.* (2007) for GNPs in PP nanocomposites showed that the aspect ratio of fillers did not significantly affect the rheology at filler concentrations up to 20 vol.%.

A possible explanation for this discrepancy is that the SSA of the GNPs varies widely in these studies. However, a systematic study on the effect of the SSA on the properties of composites containing GNPs, including their rheological properties, has not been undertaken yet. The aim of this work is to establish systematic relationships between the SSA of the GNPs and the rheological properties of their dispersions. To accomplish this goal, we produced a series of well-characterized GNPs having varying SSAs in a controlled manner, using a newly developed thermomechanical process, which exfoliates graphite [Mardlin *et al.* (2022a)]. This top-down thermomechanical exfoliation (TME) process controls the SSA through the energy input in the device during graphite exfoliation. As mentioned previously, GNPs prepared by top-down processes typically have a broad range of size distributions and surface characteristics. They are also prone to aggregation during specimen preparation, making image analysis challenging.

For such systems, including particulate-based (i.e., silica [Papadopoulou *et al.* (2020)], calcium carbonate [Osman and Attalah (2006)]) and platelet based [Vdovic *et al.* (2010), Gantenbein *et al.* (2011)], the SSA

can be used as a representative quantity, because the particle size distributions and aspect ratios are correlated to the SSA [Samoilov (2010)]. In this work we demonstrate that the SSA can be used as a parameter to correlate the properties of the particles to their rheological properties. We begin by reporting the effect of the SSA on the rheology of PEO nanocomposites, and on the rheological and electrical percolation thresholds. We estimate the aspect ratio (defined as the ratio of its major dimension to minor dimension [Gantenbein *et al.* (2011)]) of the GNP platelets using rheological models and we compare them with the values obtained from TEM image analysis. Furthermore, we use a two-phase model to quantify the polymer-filler and filler-filler interactions and to study the effect of filler content and SSA on the polymer chain dynamics and the strength of the filler network evaluated for the composite melts. Finally, we trace the conversion of graphite to the final GNP product produced from the TME process, by studying the rheological properties of the intermediates and we propose suitable rheological parameters to correlate the GNP SSA with its rheology.

## II. EXPERIMENTAL METHODS

### A. Materials and composite preparation

PEO with an average molecular weight of 20,000 g/mol, having a melting point of 62 °C, according to the manufacturer's specifications, and flake graphite (-325 mesh) were purchased from Sigma Aldrich and used as received. GNPs were produced from graphite using a patent pending TME process [Mardlin *et al.* (2022a)], which utilizes shear forces through mechanical means to exfoliate flake graphite prior to incorporation into the polymer. The delamination of graphite during the TME process has been demonstrated by XRD and TGA, and the products have been characterized in detail elsewhere [Ho and Kontopoulou (2021), Ho *et al.* (2019), Mardlin *et al.* (2022a)].

The specific surface areas of graphite and the resulting GNP powders were determined using the BET method. Samples weighing 0.2 g were degassed at 150 °C for 3 h, followed by multipoint BET physisorption analysis (Micrometrics ASAP 2010) using nitrogen at 77.35 K with relative vapour pressure varying from

0.06 to 0.9. Considering 95% confidence intervals, the error margin in the BET measurements is estimated at 3%.

The starting batch of flake graphite had an SSA of 7 m<sup>2</sup>/g and is thus noted in the following as G7. Three different batches of GNPs having final SSAs of 175 ± 5, 300 ± 9, and 430 ± 13 m<sup>2</sup>/g, were produced by TME using a torque range of 30-35 N·m. The samples are designated as GNP# x%, where # indicates the SSA and x indicates the wt.% of the filler. Another batch of GNPs, having SSA of 330 (± 10 m<sup>2</sup>/g) was produced under a torque range of 20-25 N·m. It was previously demonstrated by Mardlin *et al.* (2022a), that lower torque values result in larger amounts of unexfoliated material and thus a larger average particle size, and wider particle size distribution.

Previous work on polyamide-based composites containing graphite, expanded graphite and GNP demonstrated that the high stresses generated during melt compounding result in some in situ delamination of these fillers [Ho *et al.* (2019), Ho and Kontopoulou (2021)]. Given that the aim of this work is to assess the SSA of the as prepared GNPs, it was important to avoid further delamination. Therefore, PEO/graphite and PEO/GNP composites were prepared by mixing weighted amounts of the fillers in the low viscosity molten PEO at 70 °C and stirring by hand for approximately 5 min to avoid the generation of high stresses. Composite films containing fillers from 1 to 33 wt.% (corresponding to a vol.% of 0.53 to 20.6 vol.%, according to Eq. (1)) were cast onto heated glass petri dishes, allowed to cool to room temperature and used for further analysis.

$$\phi = \frac{\rho_m W_f}{(\rho_m - \rho_f) W_f + \rho_f} \quad (1)$$

where  $\phi$  is the filler volume fraction,  $\rho_m$  is the density of the PEO matrix (1.2 g/cm<sup>3</sup>),  $\rho_f$  is the density of graphite and GNP filler (taken as 2.3 g/cm<sup>3</sup>) and  $W_f$  is the weight fraction of filler.

## B. Contact angle measurements

The surface energy of the GNPs was measured using the contact angle method using water, diiodomethane and formamide as probe liquids. A thin film of GNPs was prepared by spray coating a 5 mg/ml GNP dispersion in dichloromethane on a Si/SiO<sub>2</sub> substrate, using a Paasche VL handheld airbrush at a nozzle pressure of 3 bar. The dispersion was sprayed 20 times on a substrate, which was heated on a hotplate at 100 °C to obtain maximum coverage and to facilitate solvent evaporation. Contact angle measurements of the sessile drops were carried out at 25 °C with a goniometer (OCA 15EC, DataPhysics Instruments, Germany), equipped with a video camera and data analysis software. The Lifshitz-van der Waals or dispersive component  $\gamma_{GNP}^{LW}$  and the acid and base interactions  $\gamma_{GNP}^+$  and  $\gamma_{GNP}^-$ , respectively, of the surface energy were calculated using the Young-Dupré equation [Van Oss (2002)]:

$$(1 + \cos\theta)\gamma_L = 2 \left( \sqrt{\gamma_{GNP}^{LW}\gamma_L^{LW}} + \sqrt{\gamma_{GNP}^+\gamma_L^-} + \sqrt{\gamma_{GNP}^-\gamma_L^+} \right) \quad (2)$$

where  $\theta$  is the contact angle measured at the triple point,  $\gamma_L$  is the total surface energy,  $\gamma_L^{LW}$  is the Lifshitz-van der Waals or dispersive component and  $\gamma_L^+$  and  $\gamma_L^-$  are the acid and base interactions respectively of the probe liquids, the values of which are available in literature [Van Oss (2002)].

## C. Dynamic light scattering (DLS)

Particle size analysis was carried out via DLS measurements performed using a Zetasizer Nano ZS instrument from Malvern. Measurements were performed on dilute dispersions in dimethyl formamide (viscosity 0.92 mPa.s & refractive index 1.43) obtained by adding up to 5 drops of 5 mg/ml dispersion of the GNPs in dimethyl formamide, and sonicating for 15 min. All measurements were performed at a temperature of 25 °C with a refractive index value of 3 for the particles; measurements were repeated three times, and the average values were reported. The spherical equivalent hydrodynamic diameter of the particles, Z-average diameter ( $Z_D$ ), was determined using the Stokes-Einstein equation (Eq. S1) by fitting the correlation function to the cumulants analysis algorithm from the Zetasizer software. The intensity-weighted particle size distribution was obtained from the Protein Analysis (non-negative least squares analysis followed by (L-curve)) algorithm.

#### D. Morphological characterization

SEM imaging was done using an FEI Quanta 650 FEG (field emission gun) ESEM (environmental scanning electron microscope) at an accelerating voltage of 5 kV and a working distance of ~8.5 mm. A gaseous secondary electron detector (GSED) was used for imaging and was carried out under a chamber pressure of 0.7 torr. Dispersions were prepared in dichloromethane at 0.5 mg/ml for graphite and 5 mg/ml for GNPs, followed by sonication for 30 and 10 min respectively. The graphite dispersions were drop cast onto a silicon wafer, whereas the GNP dispersions were centrifuged at 4500 rpm for 20 min, after which the supernatant was spin coated onto the silicon wafers. Samples were prepared for imaging by cryo-fracturing in liquid nitrogen.

TEM imaging was done using a FEI Tecnai G2 F20 S/TEM equipped with a Gatan Ultrascan 4000 CCD camera Model 895 at an accelerating voltage of 200 keV. The hydrophilic nature of the PEO facilitated imaging because it can be easily dissolved in water. Imaging for the low concentration samples was carried out by first dissolving the 3 wt.% composites in water to prepare a dilute dispersion, which was deposited on a Formvar-coated copper grid and allowed to dry overnight before imaging. For high concentration composites, samples were sectioned using a Leica Microsystems EM UC7/RC7 cryo-ultramicrotome at -90 °C to obtain ultrathin sections of ~ 70 to 100 nm thickness. The sections were collected in a sugar solution, cleaned with water and transferred to 200-mesh Cu grids with Formvar support film for imaging.

#### E. Rheological properties

Rheological measurements were carried out in a Reologica StressTech stress-controlled rheometer using a 25 mm diameter parallel plate fixture. All measurements were carried out at 70 °C, which is above the melting point of 62 °C. The measurement gap was varied between 0.5 mm to 1 mm to accommodate measurements depending upon the composition. However, measurements were not possible on GNP430 containing 33 wt.% GNPs due to high normal stresses, suggesting that smaller diameter plates may be needed for compositions containing high amounts of highly exfoliated GNPs. To ensure there is no wall slip effects, some measurements were carried out three different measuring gaps. Steady shear and dynamic

oscillatory measurements were performed on the samples. For steady shear measurements the applied stress ranged from 5 Pa to 2000 Pa. Stress sweeps were carried out from 1 to 1000 Pa at a frequency of 0.1 Hz to determine the linear viscoelastic region (LVE) of the samples. Frequency sweep measurements were carried out from 0.1 rad/s to 100 rad/s. A variable stress profile was used for each sample (ranging from 5-50 Pa, proportional to the frequency), to ensure that the measurements remained within the LVE region. SAOS measurements on dried and undried samples confirmed that drying the samples did not affect the rheology. The stability of the PEO samples was verified using time sweep measurements, along with time sweeps for the composites at 0.1 Hz and 10% strain. Structural evolution was examined using time sweeps after subjecting to pre-shear rates of 1, 10 and 100 s<sup>-1</sup> for 100 s.

#### F. Electrical conductivity

The electrical resistivity for samples with resistivities higher than 10<sup>7</sup> Ω·cm was measured using a Keithly 8009 electrometer. Samples were compression molded into thin circular sheets before measurements. Samples with resistivities lower than 10<sup>7</sup> Ω·cm were measured using the Agilent 34401 A multimeter. Samples were prepared via compression molding, and then cut into squares (1cm ×1cm) followed by coating with colloidal silver paint (supplied by Ted Pella Inc.) on both surfaces before measurement. This was done to reduce the contact resistance with the probes of the multimeter. At least three samples were measured for a given composition. Eq. 3 was used to calculate the volume conductivity  $\sigma$  (S/m) from the measured resistivities and resistances:

$$\sigma = \frac{1}{\rho} = \frac{l (m)}{R (\Omega) \times A (m^2)} \quad (3)$$

where  $\rho$  (Ω·m) is the volume resistivity,  $R$  (Ω) is the measured resistance,  $A$  (m<sup>2</sup>) is the area and  $l$  (m) is the thickness of the sample.

### III. RESULTS AND DISCUSSION

#### A. Selection of matrix

GNPs are highly prone to aggregation due to the  $\pi$ - $\pi$  stacking interactions [Li *et al.* (2008), Yang *et al.* (2012)]. Hence choosing a compatible matrix was crucial for this study to ensure good polymer/filler interactions which will facilitate the dispersion of the GNPs. PEO was chosen as the matrix based on surface energy considerations and wetting behaviour, aiming at achieving a favourable spreading coefficient.

The surface energy components of the GNPs, which were determined using Eq. 2, are as follows:  $\gamma_{GNP}^{LW} = 40.1 \text{ mJ/m}^2$ ,  $\gamma_{GNP}^+ = 0.7 \text{ mJ/m}^2$  and  $\gamma_{GNP}^- = 10.9 \text{ mJ/m}^2$ . The polar contribution of the surface energy  $\gamma_{GNP}^{AB} = 5.5 \text{ mJ/m}^2$  was calculated using Eq. 4.

$$\gamma_{GNP}^{AB} = 2\sqrt{\gamma_{GNP}^+ \gamma_{GNP}^-} \quad (4)$$

The total surface energy for GNPs  $\gamma_{GNP} = 45.6 \text{ mJ/m}^2$  was calculated as the sum of the dispersive and polar contributions, and is similar to values reported in other studies [Ho and Kontopoulou (2021), Wang *et al.* (2009)]. For PEO, the value of the total surface energy at 20 °C ( $42.8 \text{ mJ/m}^2$ ) was obtained from the literature [Mohamadi *et al.* (2019)] and was extrapolated to 70 °C to give  $\gamma_{PEO} = 38.2 \text{ mJ/m}^2$ , assuming a linear relationship with a temperature co-efficient of  $0.095 \text{ mJ/m}^2$  [Wu (1982)]. Using the polarity contribution for the total surface energy of the PEO phase ( $\gamma_{PEO}^p/\gamma_{PEO}$ ),  $x_{PEO}^p = 0.28$ , the dispersive and the polar contributions,  $\gamma_{PEO}^{LW} = 27.5 \text{ mJ/m}^2$  and  $\gamma_{PEO}^{AB} = 10.7 \text{ mJ/m}^2$  were determined respectively at 70 °C [Wu (1978)].

The interfacial energy of the PEO/GNP interface  $\gamma_{PEO/GNP} = 2.0 \text{ mJ/m}^2$  was calculated using Eq. 5 and the spreading coefficient  $S_{PEO/GNP}$  for PEO/GNP system was calculated using Eq. 6 [Texter (2014)].

$$\gamma_{PEO/GNP} = \gamma_{GNP} + \gamma_{PEO} - 2 \left( \sqrt{\gamma_{GNP}^{LW} \gamma_{PEO}^{LW}} + \sqrt{\gamma_{GNP}^{AB} \gamma_{PEO}^{AB}} \right) \quad (5)$$

$$S_{PEO/GNP} = \gamma_{GNP} - \gamma_{PEO} - \gamma_{PEO/GNP} \quad (6)$$

A positive value for  $S_{PEO/GNP} = 5.3$  was obtained indicating that spontaneous spreading or wetting of the GNPs will occur by the PEO [Texter (2014)]. These theoretical findings were supported by experimental observations of 0.5 wt.% GNP dispersions in low molecular weight (200 g/mol) PEO, which revealed that the dispersions remained stable after standing for up to 1 week.

### B. Particle size and morphology

The spherical equivalent Z-average diameter ( $Z_D$ ) and the corresponding particle diameter distributions for the GNPs determined from the DLS measurements are shown in Table I and Figure 1 respectively.  $Z_D$  decreased with GNP SSA for all GNPs prepared at 35 N.m as seen from Table I. We note that GNP330, which was prepared at a torque of 25 N.m has higher values for  $Z_D$ , along with wider particle diameter distribution, compared to GNP300, which was prepared at 35 N.m (see Figure 1). This agrees with previous observations by Mardlin *et al.* (2022a), who reported that lower torque, and thus low energy input during the TME process resulted in higher amounts of unexfoliated material.

**TABLE I.** Z-average diameter  $Z_D$ , and polydispersity index (PD)

	$Z_D$ (nm)	PD
GNP175*	812.8	0.6
GNP300*	399.4	0.3
GNP330**	529.5	0.5
GNP430*	245.2	0.5

\* processed at a torque of 35 N.m

\*\* processed at a torque of 25 N.m

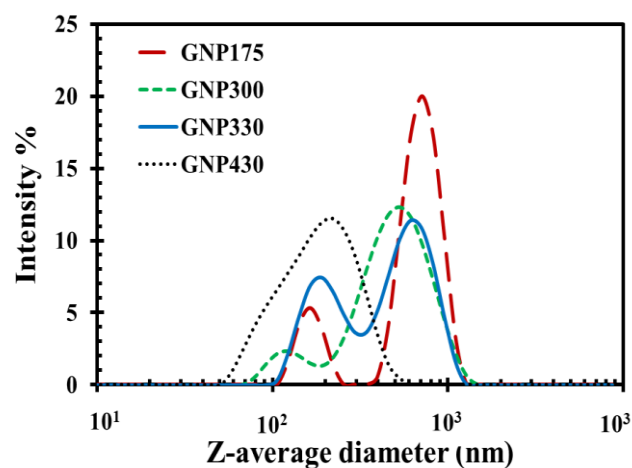


**FIG. 1.** GNP particle diameter distributions.

Figures 2(A) and (B) show the SEM images of the starting flake graphite and a representative GNP product obtained after the TME process, respectively. The graphite particles have dimensions in the tens of micrometers in length, whereas the flake-shaped GNP particles are much smaller (0.1 to 1.5  $\mu\text{m}$  in length) and thinner as a result of the shear forces subjected during the exfoliation process. Previous characterization

has shown that the GNP flakes produced by the TME process consist of 2-7 graphene layers, with the final product also containing small amounts of residual micro graphitic material [Ho and Kontopoulou (2020), Mardlin *et al.* (2022a)].

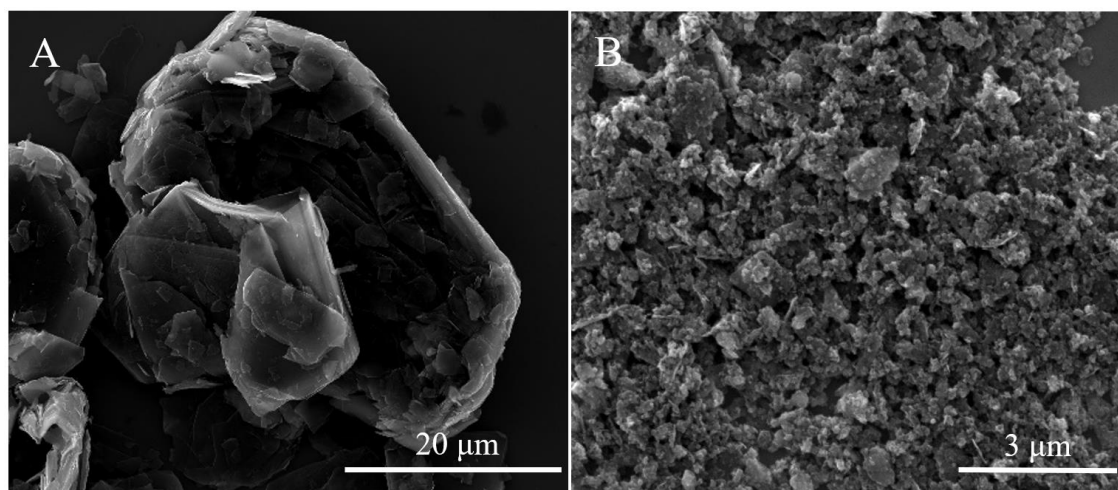


**FIG. 2.** SEM images of A) starting flake graphite B) GNP330.

The molecular weight of the PEO matrix is 20,000 g/mol, high enough for the chains to crystallize. Figure 3(A) shows the SEM image of the neat PEO matrix, which exhibits semi-crystalline structure made up of large spherulites of the order of a 100  $\mu\text{m}$ . Figures 3(B) and 3(C) show GNP175 composites containing 8 wt.% and 15 wt.% GNPs. The GNPs are present both as individual flakes and as aggregates and are distributed throughout matrix. A residual micrographite segment is also visible in Figure 3(B). The incorporation of GNPs into the PEO matrix disrupts its crystalline structure, since the particles act as barriers to the formation of large PEO crystals and may also serve as nucleating agents, thereby increasing crystallisation rates and reducing crystal sizes. Similar observations were reported in GNP and MWCNT nanocomposites in PP and PA matrices [Li *et al.* (2011), Bhattacharyya *et al.* (2003), Mardlin *et al.* (2022b)]. From Figure 3(B), it is seen that at 8 wt.% filler content, the GNP175 fillers are present in small clusters which are separated from each other. When the GNP content is increased to 15 wt.% in Figure 3(C), the GNP175 flakes become more concentrated. As the concentration increases further, conductive

pathways are formed, leading to the manifestation of an electrical percolation threshold, as analyzed in the section below.

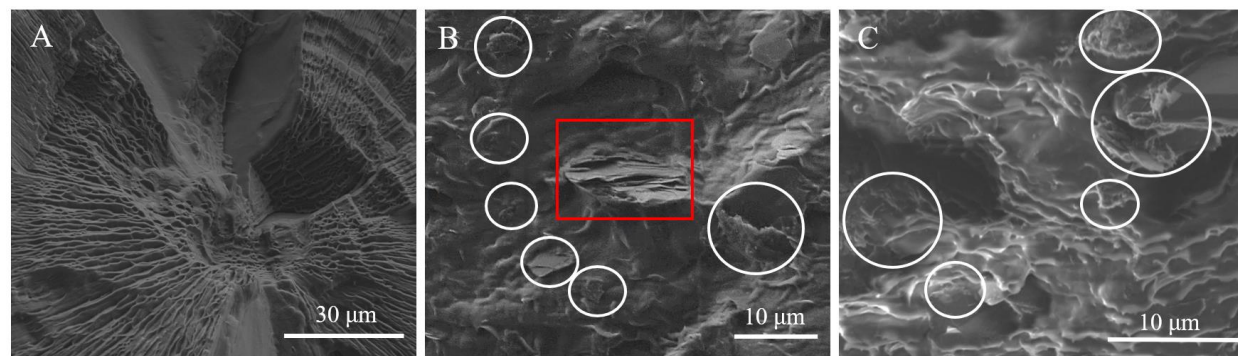


**FIG. 3.** SEM images of cryo-fractured surfaces of A) neat PEO, B) 8 wt.% GNP175, C) 15 wt.% GNP175. White circles show GNP flakes and the red box shows a piece of unexfoliated micrographite.

### C. Electrical conductivity

Figure 4 shows the electrical conductivity,  $\sigma$ , versus filler volume fraction,  $\phi$ , for the graphite and GNP samples having different SSAs. Looking specifically at low  $\phi$ , it is worth noting that graphite samples demonstrate higher conductivity values. This is attributed to the larger flake size of the graphite material (as seen in Figure 2A), which results in lower intrinsic resistance per particle [Ruschau *et al.* (1998)], favours direct contact between filler particles in the matrix, and therefore facilitates electron hopping necessary for conductivity. Ho and Kontopoulou (2021) invoked the “island-bridge” model [He *et al.* (2017)] to explain this behaviour in expanded graphite/polypropylene composites.

At low  $\phi$ , we observe an initial decrease in conductivity with filler content for all composites, which can be attributed to the trapping of the free charge carriers present in the PEO due to the presence of filler particles [Baeza *et al.* (2015)], while it appears that increasing the SSA of the fillers aggravates this phenomenon. When comparing GNP175, GNP300 and GNP430, which were prepared at the higher torque of 35 N.m, we observe that increasing SSA results in lower conductivity at low  $\phi$ , whereas GNP330, which was

produced using a lower torque is closer to GNP175, presumably because it contains larger average particle sizes.

Above a critical concentration, defined as the electrical percolation threshold  $\phi_c$ , the electrical conductivity of the composites increases by orders of magnitude with increasing  $\phi$ . This transition corresponds to the formation of a conductive filler network, where electron transport can occur through electron hopping across the graphite or GNP network and through electron tunneling [Ho and Kontopoulou (2021), Kota *et al.* (2007)].

Quantitative comparisons can be provided by the empirical electrical percolation model given by Eqs. 7a and 7b respectively below and above this critical concentration  $\phi_c$  [Vasileiou *et al.* (2013)]:

$$\sigma = \sigma_{matrix} \left( \frac{\phi_c - \phi}{\phi_c} \right)^{-u} \quad , \quad \phi < \phi_c \quad (7a)$$

$$\sigma = \beta \left( \frac{\phi - \phi_c}{1 - \phi_c} \right)^v \approx \beta (\phi - \phi_c)^v \quad , \quad \phi > \phi_c \quad (7b)$$

where  $\sigma$  and  $\sigma_{matrix}$  (S/m) are the electrical conductivities of the composite and the matrix respectively, and  $u$ ,  $\beta$  (S/m) and  $v$  are fitting parameters to the electrical percolation model. The model fits are shown in Figure 4, and the values of  $\phi_c$  for each of the PEO composites, are summarized in Table II. As a general trend, it is observed that the filler SSA has a significant influence on both  $\phi_c$  and the maximum conductivity, with  $\phi_c$  decreasing from 10.4 vol.% for graphite to 8.2 vol.% at SSAs above 300 m<sup>2</sup>/g. Conversely, the critical exponent,  $v$ , increases from 2.3 to 3.9 and levels off. While the theoretical values of the critical exponent  $v$  range from 1.6 to 2.0 for three-dimensional percolating systems, several studies have reported experimental values ranging from 1.32 to 5.35 for GNP composites [Sabzi *et al.* (2013), Kashi *et al.* (2018), Mardlin *et al.* (2022b), Canales *et al.* (2016), Gao *et al.* (2018)]. The increase in the maximum conductivity of the GNP composites with increasing GNP SSA can be attributed to the formation of a greater number of conductive paths, and to lower particle-particle contact resistance (due to enhanced van der Waals interactions) in the presence of the exfoliated GNP particles [Ruschau *et al.* (1998), Yang *et al.* (2011)].

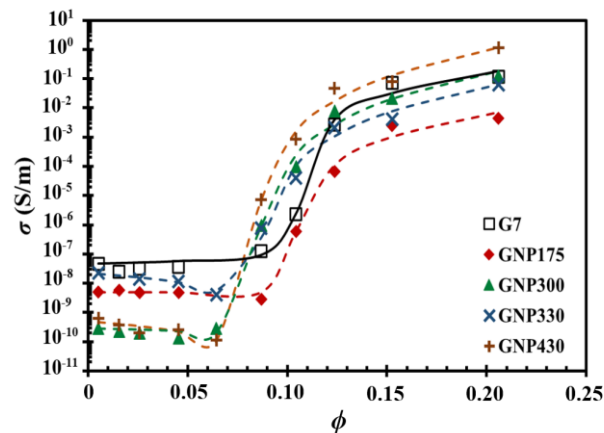


**FIG. 4.** Electrical conductivity  $\sigma$  versus filler volume fraction  $\phi$  for graphite and GNP fillers having different SSAs. The lines are model fits to Eq. 7.

**TABLE II.** Electrical percolation threshold  $\phi_c$ , critical exponent  $\nu$  (from Eq. 7), maximum conductivity  $\sigma_{max}$ , and rheological percolation threshold  $\phi_{per}$  and critical exponent  $b$  (from Eq. 8)

Filler	$\sigma_{max}$ (at 33 wt.%) S/m	$\phi_c$		$\nu$	$\phi_{per}$		$b$
		vol.%	wt.%		vol.%	wt.%	
G7	$1.2 \times 10^{-1}$	10.4	17.9	2.3	12.4	21.0	0.2
GNP175	$4.5 \times 10^{-3}$	10.1	17.5	2.7	12.3	21.0	0.4
GNP300	$1.3 \times 10^{-1}$	8.2	14.4	3.9	10.4	18.0	3.4
GNP330	$6.2 \times 10^{-2}$	8.2	14.4	3.8	10.9	18.8	2.6
GNP430	$1.2 \times 10^0$	8.1	14.3	3.9	5.4	9.7	6.6

#### D. Steady shear viscosity and SAOS characterization

The steady shear viscosity measurements are shown in Figure 5 together with the complex viscosity data obtained through SAOS experiments. The flow curves of the neat PEO matrix used in this work follow Newtonian behaviour. Therefore, any deviations from this Newtonian plateau in the filled sample measurements can be unambiguously attributed to the presence of the graphite or GNP particles. In all cases, composites containing up to 8 wt.% filler follow a Newtonian behaviour, with very moderate increase in the viscosity due to the hydrodynamic effect of the particles. Furthermore, SAOS time sweeps, shown in Figure S1(A) show that the neat PEO and the composites have stable response as a function of time.

As seen in Figure 5, the Cox-Merz rule is valid up to 8 wt.% for all composites, and it begins to fail for samples containing 15 wt.% filler and above; this coincides with the onset of deviations from Newtonian behaviour. The latter are attributed to the decrease in the interparticle distances at higher concentrations, and to the formation of an elastic structure in the composites [Claypole *et al.* (2020)]. Failure of the Cox-Merz rule is observed commonly in systems exhibiting structure formation that is typically preserved under LVE measurements but is affected by shear [Shafiei-Sabet *et al.* (2012)]. Positive deviations of the steady shear viscosities from the complex viscosities at low shear rates/frequencies have been observed in particulate systems, including layered silicates, GNPs, CNT and glass microspheres [Kim *et al.* (2005), Nazockdast *et al.* (2008), Becker *et al.* (2003), Claypole *et al.* (2020), Song *et al.* (2006), Kaully *et al.* (2007), Carotenuto *et al.* (2021)]. It should be noted that GNP-containing composites (Figure 5B) showed more pronounced deviations compared to their graphite containing counterparts (Figure 5A).

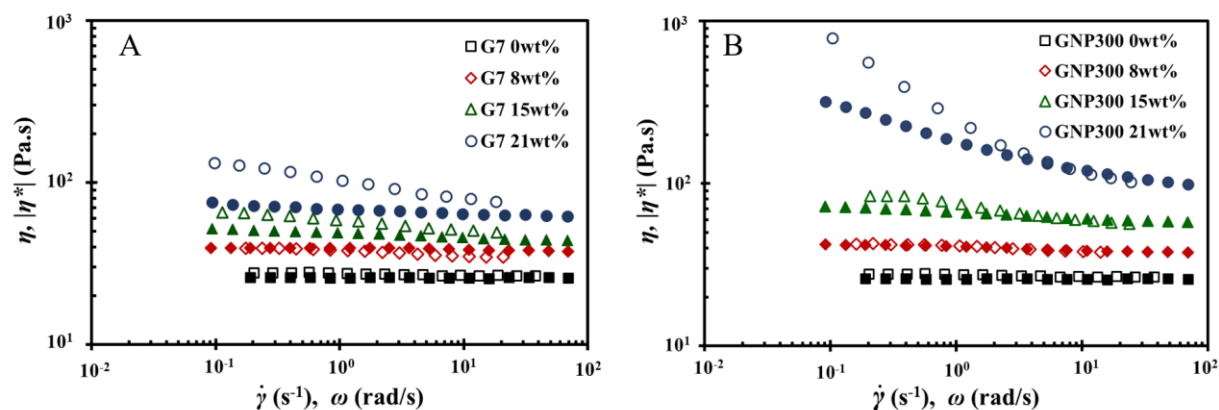


**FIG. 5.** Plots of steady shear viscosity  $\eta$  versus shear rate (open data points) and complex viscosity  $|\eta^*|$  versus angular frequency (closed data points) for A) graphite and B) GNP300 composites measured at a temperature of 70 °C.

As seen in Figure 5, the deviations from the Cox-Merz rule are pronounced at low shear rates, up to a shear rate of  $10 \text{ s}^{-1}$ , suggesting that shear rate affects the structure of the composites. Further insight on the effects of shear rate can be gleaned by looking into time sweeps after preshearing. Figure S1(B), shows pronounced time-dependency at a low pre-shearing rate of  $1 \text{ s}^{-1}$ , presumably because of particle aggregation

[Wang *et al.* (2016), Li *et al.* (2021), Zhang and Archer (2002), Helal *et al.* (2019)], which results in a higher complex viscosity at the start of the time sweep. On the other hand, shear rates of  $10 \text{ s}^{-1}$  and above lead to an alignment of the platelets, resulting in lower viscosity, and a different response during the time sweep.

SAOS experiments reveal significant deviations from terminal behaviour in the storage modulus  $G'$  slope along with loss of the Newtonian plateau above 15 wt.% filler is seen in Figure S3 and 6(A) respectively. Representative plots for the GNP300 composites, are shown in Figures 6(A-B) (plots for graphite and other GNP composites can be found in the SI, Figures S2-S4).

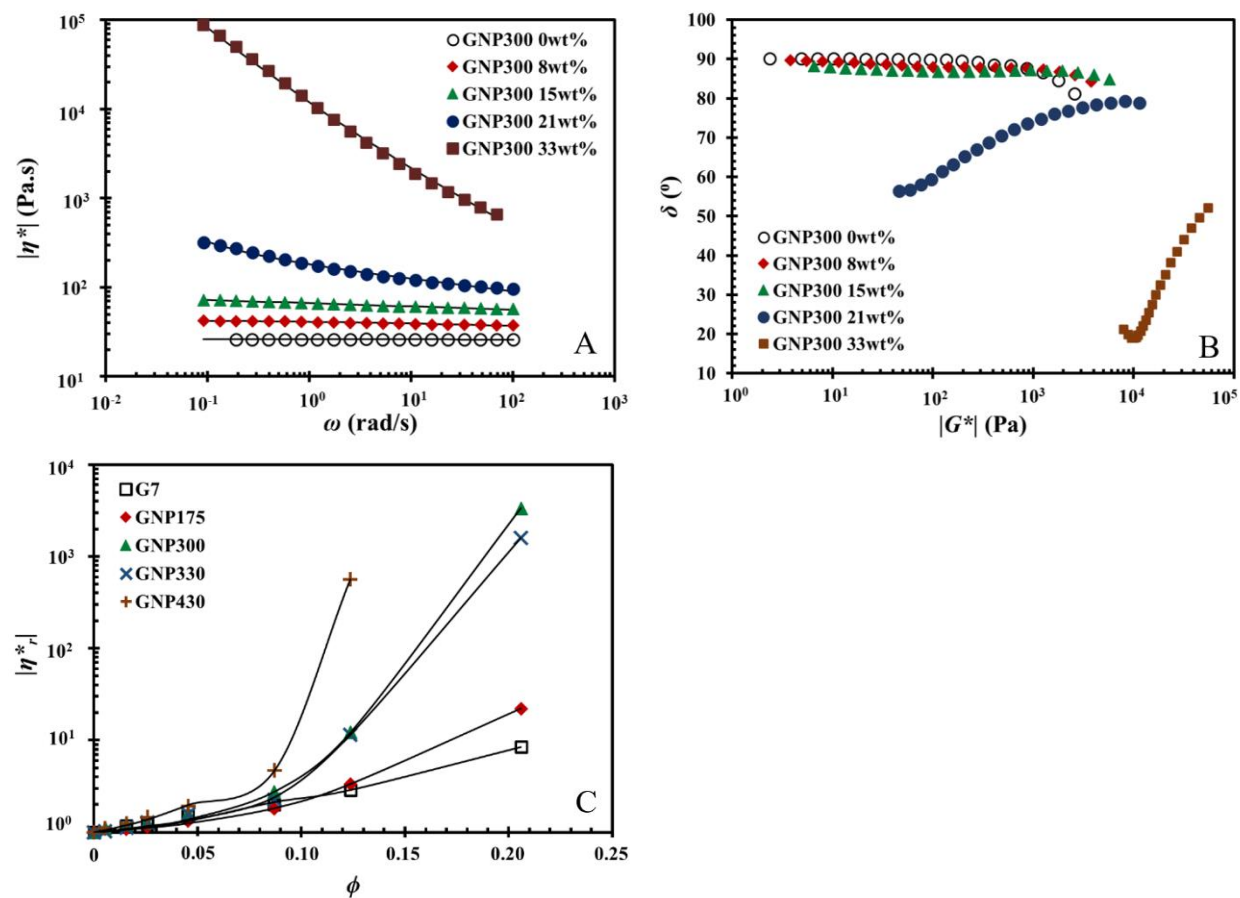


**FIG. 6.** A) Complex viscosity  $|\eta^*|$  versus angular frequency  $\omega$  (The data points represent measurements whereas the solid lines represent the Cross model Eq. S2 and Berzin model Eq. 11 fits to data, at low and high  $\phi$  respectively), B) van Gurp-Palmen plots of phase angle  $\delta$  versus complex modulus  $|G^*|$  as a function

of the filler concentration for GNP300 composites and C) reduced values of  $|\eta^*|$  versus  $\phi$  as a function of SSA (The lines are the best fits obtained using Eq. 8). All measurements are conducted at 70 °C.

The van Gurp-Palmen plots (phase angle  $\delta$  versus complex modulus  $|G^*|$ ) shown in Figure 6(B) also exhibit a divergence above 15 wt.%. These plots are very sensitive to the formation of filler-network structures within the melts. Neat PEO and composite melts at low concentrations exhibit  $\delta(\omega, \phi)$  close to 90°. At concentrations higher than 15 wt.% the G7 and GNP composite melts exhibit a sizeable decrease in  $\delta(\omega, \phi)$  at low values of  $|G^*|$ , demonstrating that the materials transition from viscoelastic liquid-like behaviour to a viscoelastic solid-like response. This decrease in phase angle  $\delta(\omega, \phi)$  is ascribed to the evolution of the filler network that imparts elasticity to composite melts [Kashi *et al.* (2018), Wu *et al.* (2010), Abdel-Goad *et al.* (2007)], and coincides with the rheological percolation threshold.

The elastic properties of space filling aggregate networks formed above the rheological percolation threshold can be described by the rheological percolation model (Eq. 8), which depicts the power-law dependence of rheological properties on  $\phi$  [Iqbal *et al.* (2016), Vermant *et al.* (2007), Zohrevand *et al.* (2014)]. The reduced complex viscosity at the lowest measured frequency of 0.1 rad/s given by  $|\eta_r^*| = |\eta^*|/|\eta_m^*|$  ( $|\eta_m^*|$  is the complex viscosity of the matrix) was used in Eq. 8a and 8b to fit data below and above the rheological percolation threshold respectively as shown in Figure 6(C):

$$|\eta_r^*| \approx \left( \frac{\phi_{per} - \phi}{\phi_{per}} \right)^{-c} \quad \phi < \phi_{per} \quad (8a)$$

$$|\eta_r^*| \approx \alpha \left( \frac{\phi - \phi_{per}}{\phi_{per}} \right)^b \quad \phi > \phi_{per} \quad (8b)$$

where  $c$  and  $b$  are power law scaling exponents below and above  $\phi_{per}$  respectively and  $\alpha$  is a fitting parameter. The  $\phi_{per}$  values determined from Eqs. 8a and 8b are reported in Table II along with the scaling exponent  $b$ . Consistent with the electrical percolation threshold  $\phi_c$ , the rheological percolation threshold concentration  $\phi_{per}$  and  $b$  also depend on the SSA; increasing SSA results in lower  $\phi_{per}$  and higher  $b$ , suggesting that higher SSAs facilitates the formation of elastic, space-filling networks at lower  $\phi$ . GNP300

and 330, have similar  $\phi_{per}$  values, considering the statistical error margin in both the BET measurement, and the rheological measurements. Furthermore, GNP300, was processed at a higher torque of 35 N.m and has smaller average particle size compared to GNP330 (see also Table I), thus promoting network formation [Chen *et al.* (2015)].

The value of the exponent  $b$  gives critical insight into the stress bearing mechanisms of these percolated systems. Sabzi *et al.* (2013), Gao *et al.* (2018) and Surve *et al.* (2006) reported that a critical exponent value of  $b < 2.1$ , as seen for G7 and GNP175 composites, indicates that the stress bearing mechanism is mediated via polymer bridging between the filler particles, whereas for  $b > 3.75$ , as is the case for GNP430 composites, direct particle-particle network serves as the stress bearing mechanism. Based on their intermediate  $b$  values, we expect that GNP300 and GNP330 composites would have some polymer bridging and some direct particle-particle networks responsible for the stress propagation.

It is interesting to note that despite the high SSA and disc/platelet shaped nature of graphite and GNP fillers, these nanocomposites exhibit a modest rheological response even at high  $\phi$  compared to other nanocomposite systems. The rheological percolation threshold values are also much higher compared to CNTs (~0.6-2.5 vol.%) [Wu *et al.* (2010)], or other layered fillers such as nanosilicates (~1.35 vol.%) [Eslami *et al.* (2010)]. This may be explained by a considerable lubrication effect seen for graphite and GNP fillers facilitated by hydrodynamic slip and orientation of platelets in the direction of shear flow as reported by Kotsilkova *et al.* (2021). The lubrication effect of graphite and GNPs have also been previously reported in several tribological studies [Baptista *et al.* (2016), Kazemi-Khasragh *et al.* (2020), Nieto *et al.* (2012)].

Based on the results presented above, we hypothesize that the filler SSA affects the polymer-filler interactions at low loadings, and the filler-filler interactions at higher loadings. We therefore present the rheological results on the effects of SSA in two sections: low filler concentrations (i.e. non-interacting particles) and high filler concentrations (aggregated, or interacting particles, where filler-filler interactions dominate).

This is the author's peer reviewed, accepted manuscript. However, the online version of record will be different from this version once it has been copyedited and typeset.  
PLEASE CITE THIS ARTICLE AS DOI: 10.1122/1.5111111

### E. Low filler concentrations (non-interacting particles)

TEM images of graphite and GNP flakes deposited from low concentration dispersions of the composites in water are shown in Figure 7. Figure 7(A) shows a micron-sized flake of graphite, together with the presence of stacked platelets (Figure 7 B). Figures 7(C-D) show transparent GNPs made up of few layers of graphene in the form of nano flakes, and irregular-shaped platelets, which are likely the result of fragmentation and erosion during the TME process [Mardlin *et al.* (2022a)]. The particle size distribution of the GNPs based on the lateral sizes obtained from these TEM images are shown in Figure S6. These images are representative of the smaller particle size ranges that are present in these samples that contain low concentrations of GNPs.

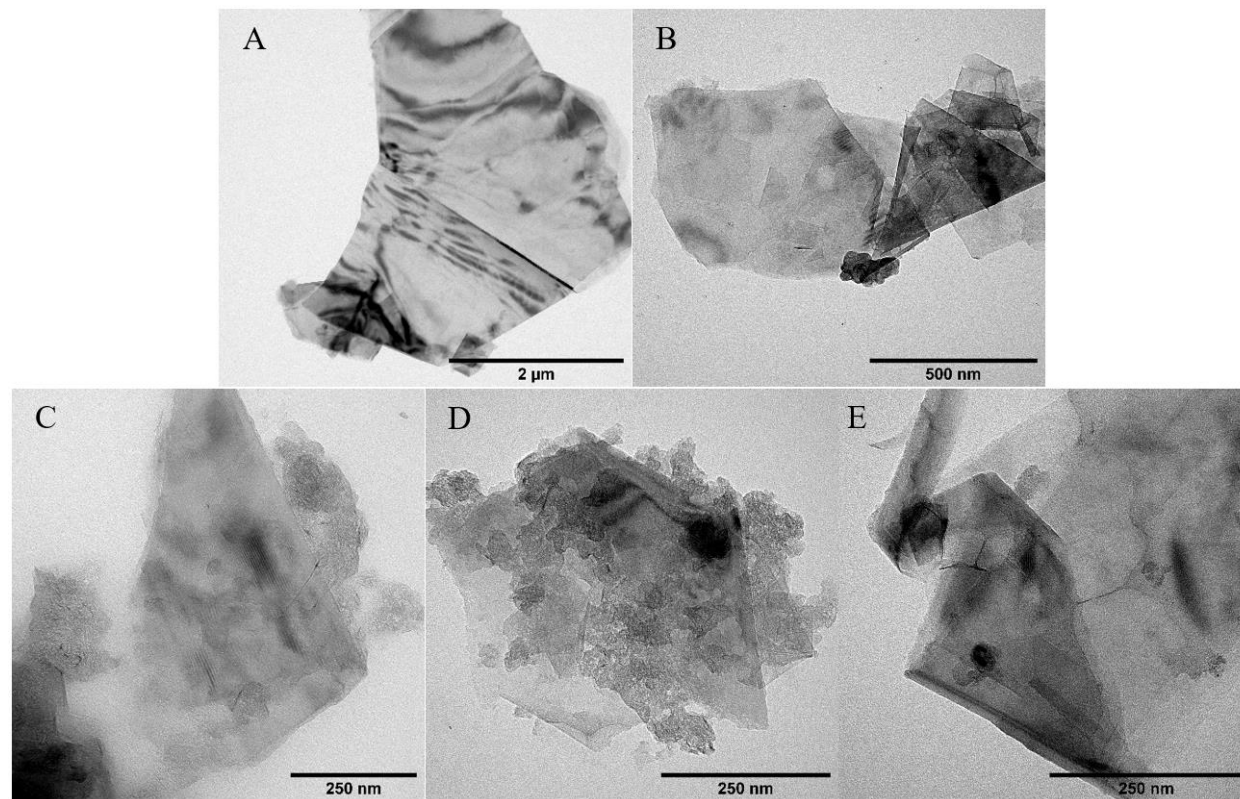


**FIG. 7.** TEM images of A) & B) graphite, C) GNP175 D) GNP330 E) GNP430.

The neat PEO, having a molecular weight of 20,000 g/mol, exhibits terminal flow behaviour ( $G' \propto \omega^2$  at low  $\omega$ ). The entanglement molecular weight  $M_e$  of PEO ranges from  $\sim 1730 - 2000$  g/mol and the critical

molecular weight for entanglements,  $M_c$  ranges from  $\sim 4000 - 5,870$  g/mol [Anderson and Zukoski (2009), Fetters and Colby (2007)]. Therefore, the PEO used in this work is above the entanglement limit. At low filler concentrations the hydrodynamic effects dominate the rheological response of the composites. Figures 8(A) shows the complex viscosity  $|\eta^*|$  versus angular frequency  $\omega$  plot at concentrations up to 8 wt.% for the GNP300 composites (see Figure S7 for graphite and other GNP composites and S8 for the  $G'$  plots). With the addition of fillers, the complex viscosity and the elastic modulus of the composites increase as result of the filler hydrodynamic effects, and slight particle-particle interactions, which cause increased friction [Baeza *et al.* (2015), Song and Zheng (2010), Vermant *et al.* (2007)].

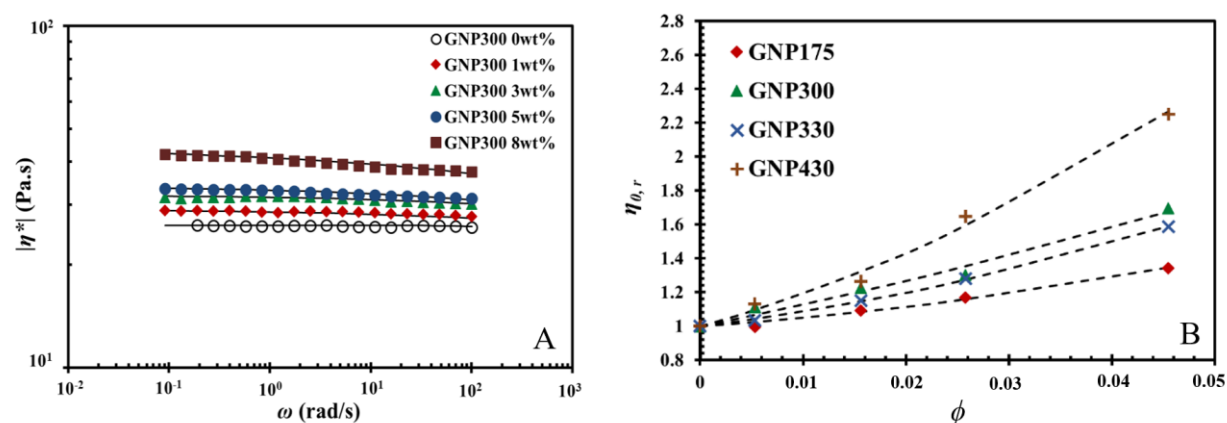


**FIG. 8.** A) Complex viscosity  $|\eta^*|$  versus angular frequency  $\omega$  at 70 °C (The data points represent measurements, and the solid lines represent the Cross model fit Eq. S2) and B) reduced zero-shear viscosity  $\eta_{0,r}$  versus  $\phi$  for GNP samples at low concentrations (The dashed lines represent the Utracki and Lyngaae-Jørgensen (2002) model Eq. 9 fit to the relative viscosity data).

The effect of  $\phi$  on  $|\eta^*|$  becomes more pronounced with increasing SSA, as shown in Figure S7. This is also summarised in Figure 8(B) in terms of the reduced zero-shear viscosity  $\eta_{0,r}$  (ratio of the zero-shear viscosity of composite to that of the matrix) obtained by fitting the Cross model (Eq. S2) to the complex viscosity data of Figures 8(A) and S7. The Cross model parameters obtained from fitting compositions up to 8 wt.% are given in Table S1.

In this region where there are minimal interactions between the particles, the average aspect ratio of the fillers can be estimated by considering the effect of the particles on the viscosity. The reduced zero-shear viscosity  $\eta_{0,r}$  in Figure 8(B) was fit to a second order Einstein-type equation proposed by Utracki and Lyngaae-Jørgensen (2002) given by Eq. 9 for low concentration suspensions of anisometric particles; a similar equation was first proposed by Guth and Gold (1938):

$$\eta_{0,r} = 1 + [\eta]\phi + k([\eta]\phi)^2 \quad (9)$$

where  $[\eta]$  is the intrinsic viscosity and  $k$  is the interaction constant. From the intrinsic viscosity values determined above, the aspect ratio  $p$  of the GNP filler was predicted using Eq. 10, which is applicable for disks or platelets [Beuguel *et al.* (2018), Utracki and Lyngaae-Jørgensen (2002)]:

$$[\eta] = 2.5 + 0.025(1 + p^{1.47}) \quad (10)$$

The  $[\eta]$ ,  $k$ , and  $p$  values determined for the GNP composites are shown in Table III. The aspect ratio for the GNPs, which for platelets is defined as the longest dimension of the particle to its thickness, varies between 19 to 76; this is within the range of aspect ratios estimated for GNPs in previous work [Ho and Kontopoulou (2021), Ho *et al.* (2019)]. The filler concentrations  $\phi_{m,plate}$ , up to which the platelets can rotate freely, determined from Eq. S3 [Utracki and Lyngaae-Jørgensen (2002)] are also shown in Table III.

The values obtained from the model show that the aspect ratios of the GNP fillers generally increase with GNP SSA, whereas the  $\phi_{m,plate}$  values decrease with increasing GNP SSA. It should be noted however that GNPs produced by top-down approaches have broad particle size distributions, and therefore these are only general trends. As shown in Table III, GNP330, which was processed at a lower torque and therefore had larger particle sizes and a broader particle size distribution, displays lower aspect ratio, and larger  $\phi_{m,plate}$  compared to GNP300.

This is the author's peer reviewed, accepted manuscript. However, the online version of record will be different from this version once it has been copyedited and typeset.  
PLEASE CITE THIS ARTICLE AS DOI: 10.1122/1.50000531

**Table III.** Intrinsic viscosity  $[\eta]$ , interaction constant  $k$ , aspect ratio  $p$  and  $\phi_{m,plate}$  obtained by fitting Eq. 9, 10 and S3. GNP175, 300 and 430 were processed at a torque of 35 N·m and GNP 330 was processed at 25 N·m.

Sample	$[\eta]$	$k$	Aspect ratio $p$	$\phi_{m,plate}$
GNP175	4.35	3.76	19	0.052
GNP300	12.21	0.38	58	0.017
GNP430	16.96	0.83	76	0.013
GNP330*	8.25	1.54	41	0.026

\*processed at 25 N·m

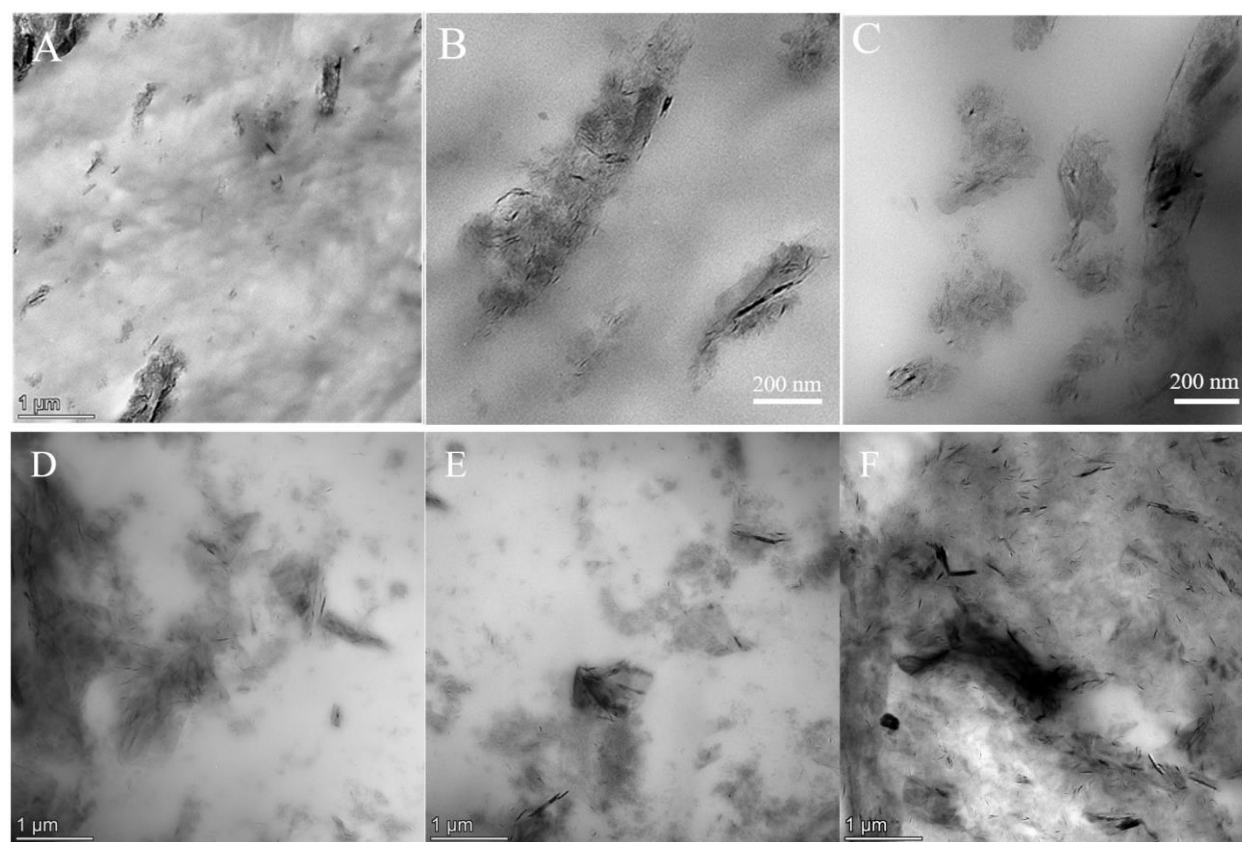


**FIG. 9.** TEM images of A) and B) GNP430 8 wt.%, C) GNP330 8 wt.%, D) and E) GNP430 21 wt.% and F) GNP330 21 wt.% composites.

As the concentration increases to 8 wt.%, the van der Waals interactions (specifically,  $\pi$ - $\pi$  interactions) between the particles lead to the formation of sub-micron sized stacks of layers (or tactoids) within the melt, as seen in Figures 9(A-C). This results in more pronounced hydrodynamic effects, however the tactoids remain relatively isolated, and the melt presents minimal shear thinning, as shown in Figure 8(A).

#### F. High filler concentrations (aggregated or interacting particles)

At filler concentrations above 15 wt.%, noticeable deviations from terminal flow behaviour appear in  $|\eta^*|$  and  $G'$ . These are attributed to the formation of larger tactoids, which begin to interact with neighboring particles. The complex viscosity dependence on frequency in the low frequency region scales as  $|\eta^*| \propto \omega^{n-1}$ . The  $n$  values along with the terminal region slopes for the elastic modulus  $m$  and viscous modulus  $o$ , are shown in Table S2 along with complex viscosity values at the lowest measured frequency  $|\eta^*|_{\omega=0.1\text{rad/s}}$ . Deviation from Newtonian behavior (corresponding to  $n$  equal to 1) is seen with increasing  $\phi$  along with the decrease in the rest of the slopes, indicative of nonterminal behaviour.

As the interparticle distances decrease, at compositions above the percolation threshold (see Table II), the tactoids start to form 3-D interconnected networks, as shown in Figures 9(D-F) and exhibit pronounced yielding behaviour, demonstrated by the complex viscosity data in Figures 6(A), 10(A), S2 and S9. To obtain an estimate of the yield stress, the complex viscosity  $|\eta^*|$  in Figure 6(C) is fit to the Berzin model given by Eq. 11 (shown by the solid lines):

$$|\eta^*| = \frac{\sigma_0}{\omega} + \eta_0 [1 + (\lambda_2 \omega)^a]^{-\frac{n_2-1}{a}} \quad (11)$$

where  $\omega$  (rad/s) is the angular frequency,  $\sigma_0$  (Pa) is the yield stress,  $\eta_0$  (Pa.s) is the zero-shear viscosity,  $\lambda_2$  (s) is the characteristic time or average relaxation time,  $n_2$  is the power law index and  $a$  is the Yasuda parameter [Sethy *et al.* (2020), Vergnes (2011)]. From the model fit, finite yield stress values were obtained as shown in Table IV (see Table S3 for other Berzin model parameters).

**Table IV.** Yield stress  $\sigma_0$  values determined from the Berzin model (Eq. 11)

Sample	Yield Stress, $\sigma_0$ (Pa)			
	8 wt. %	15 wt.%	21 wt.%	33 wt.%
Graphite	0.0	0.0	0.5	6.8
GNP175	0.0	0.0	0.8	22.9
GNP300	0.0	0.0	8.4	5943.7
GNP330	0.0	0.0	10.0	3100.8
GNP430	0.0	1.9	1362.2	*

\*measurement was not possible due to high normal forces

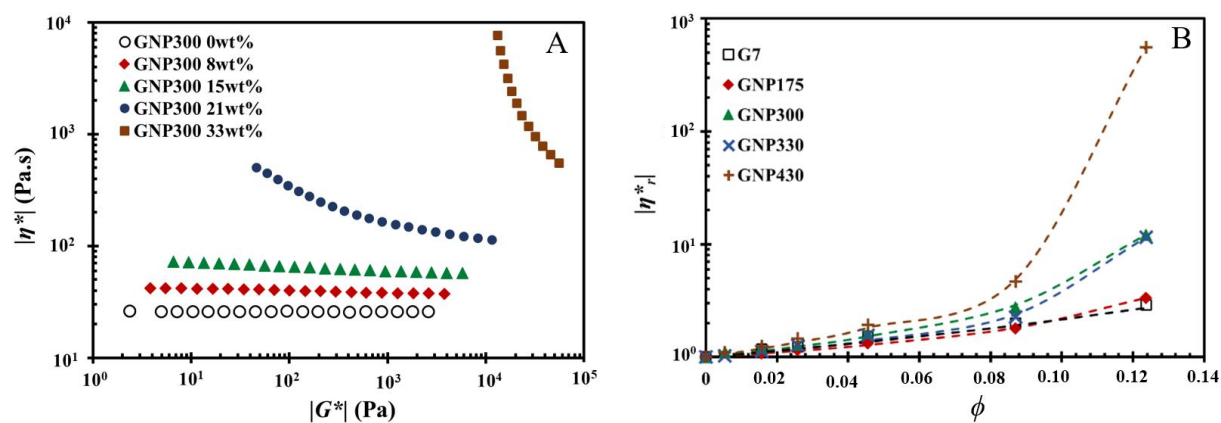


**FIG. 10.** A) Complex viscosity  $|\eta^*|$  versus complex modulus  $|G^*|$  for GNP300 composites and B) reduced complex viscosity  $|\eta_r^*|$  versus  $\phi$  for graphite and GNP composites at high  $\phi$ . The dashed lines represent the Krieger-Daugherty model (Eq. 12) fit to the reduced viscosity data.

Vergnes (2011) argued that the level of exfoliation of layered fillers could be traced by the yield stress values, which represent the extent of interactions between the nanofillers. From Table IV it is apparent that the yield stress values of the composites and the onset of yielding scales with the filler SSA, indicating that GNPs with higher SSA are better exfoliated and form stronger filler networks of highly interacting particles.

The aspect ratios of the aggregated tactoids, determined from analysis of the TEM images of GNP composites at high  $\phi$ , are shown in Table V. Here the aspect ratios are defined as the ratio of length to

width of the aggregates, as they form 3D structures. The results from the image analysis reflect the large distribution of particle sizes and aspect ratios.

The Krieger-Daugherty model (Eq. 12) was used to fit the reduced complex viscosity  $|\eta_r^*|$  data over the entire range of  $\phi$  (see Figure 10 B). The filler aspect ratio is then determined using Eq. 13 [Beuguel *et al.* (2018)]:

$$|\eta_r^*| = \left(1 - \frac{\phi}{\phi_{max}}\right)^{-[\eta]\phi_{max}} \quad (12)$$

$$[\eta] = 3.02 + 0.321p \quad (13)$$

where  $\phi_{max}$  is the maximum packing fraction. Here  $p$  represents the “hydrodynamic” aspect ratio of the tactoids [Vermant *et al.* (2007)]. The aspect ratios, shown in Table IV, are in good agreement with the average values determined from the TEM image analysis (defined as length/width). The increase in aspect ratio and decrease in  $\phi_{max}$  with increasing GNP SSA are attributed to the higher surface area, which results in enhanced filler network formation [Vermant *et al.* (2007)]. As seen with previous results, due to its larger average particle size and distribution, GNP330 has lower aspect ratio, compared to GNP 300.

**Table V.** Intrinsic viscosity  $[\eta]$ , maximum packing fraction  $\phi_{max}$  and aspect ratio  $p$  obtained by fitting Eq. 12 and 13. GNP175, 300 and 430 were processed at a torque of 35 N·m and GNP 330 was processed at 25 N·m.

Sample	$[\eta]$	$\phi_{max}$	Aspect ratio $p$	Aspect ratio $p$ from TEM Images
GNP175	4.6	0.15	5	7.1 ± 6.6
GNP300	7.4	0.13	14	11.9 ± 7.2
GNP430	10.6	0.12	24	15.7 ± 13.6
GNP330*	6.1	0.13	9	10.1 ± 7.6

\*processed at 25 N·m

### G. Two-phase model

As mentioned above, the rheological behaviour of the graphite and GNP dispersions in PEO can be differentiated into two categories: low filler concentrations  $< 8$  wt.% where particles are non-interacting and higher filler concentrations  $\geq 15$  wt.% where the particles are increasingly interacting with each other and eventually form percolated networks. To better elucidate these regions, we use the two-phase model proposed by Song and Zheng (2010, 2011) to quantitatively describe the rheological response of filled polymer melts. According to the two-phase model, the nanocomposite melt consists of two phases: the filler phase consisting of individual particles and/or aggregates including the interface consisting of immobilized polymer (possibly due to physical adsorption or confinement between filler particles); and the bulk polymer phase. Addition of hard and not very deformable particles into a polymer matrix which is soft and highly deformable leads to an increase in the complex modulus  $|G^*(\omega, \phi)|$  of the filled melt. At low filler concentrations this can be attributed to hydrodynamic effects arising from the concentration of the global straining motion in the polymer phase resulting in a so-called “strain amplification effect” which is proportional to the filler volume fraction and is described by Eq. 14 [Song and Zheng (2010)]:

$$|G^*(\omega, \phi)| = A_f(\omega, \phi)|G_m^*(\omega)| \quad (14)$$

where  $|G_m^*|$  is the complex modulus of the matrix and  $A_f$  is the strain amplification factor. Figure S10 A shows the  $|G^*|$  versus  $|G_m^*|$  curves for the GNP300 composites. Up to 8 wt.%, the  $|G^*|$  versus  $|G_m^*|$  plotted on a log-log scale has a power law exponent approximately equal to 1, indicating that Eq. 14 describes the hydrodynamic effects well. As described earlier, this is the region of non-interacting particles.

At concentrations beyond 8 wt.%, there is an additional contribution of the filler phase  $|G_f^*(\omega, \phi)|$  to Eq.14 arising from direct contact between the filler domains or through polymer bridging between neighbouring aggregates, which lead to formation of larger structures. These structures result in a more complicated rheological response that can no longer be described by simple hydrodynamic equations. At higher concentrations, the following equations apply:

$$\frac{G'(\phi, \omega)}{G'_m(\omega)} = A_f(\phi) + R'_f(\phi)[G'_m(\omega)]^{n_3-1} \quad (15a)$$

$$\frac{G''(\phi, \omega)}{G''_m(\omega)} = A_f(\phi) + R''_f(\phi)[G''_m(\omega)]^{n_3-1} \quad (15b)$$

where  $R'_f$  and  $R''_f$  are scaling factors that represent elastic and viscous contributions of the filler phase respectively and exponent  $n_3$  is an independent fitting parameter that depicts the transition from pure liquid ( $n_3 = 1$ ) to pure solid ( $n_3 = 0$ ) response. The  $G''/G'_m$  curve is shifted horizontally by a factor  $z$  to allow Eq. 15a and b to be solved simultaneously to determine values of  $A_f$ ,  $R'_f$  and  $R''_f$  and  $n_3$ . The fits are shown in Figure S10 B. All the fitted values for the graphite and GNP systems are reported in Figures 11 (A-B) and S10 (C-D).

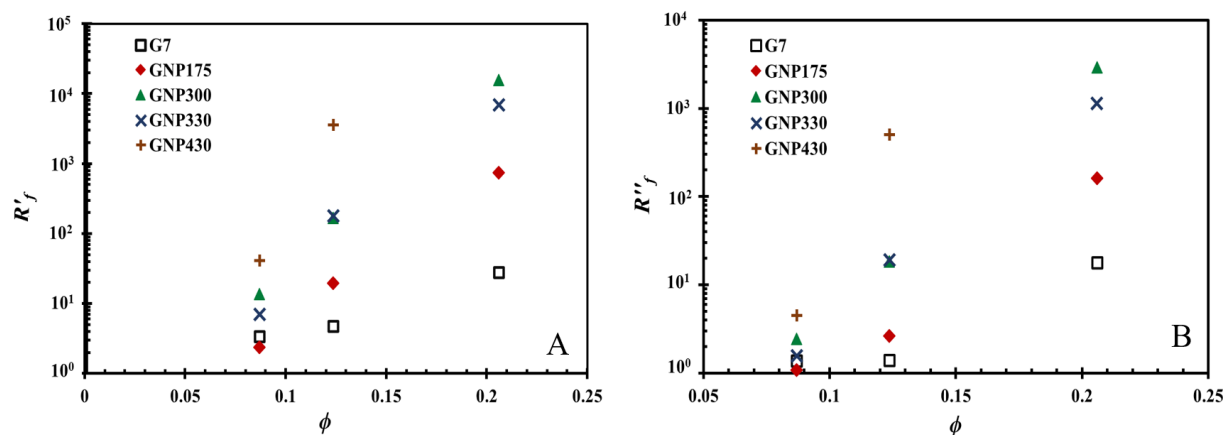


**FIG. 11.** Two phase model parameters A)  $R'_f$  and B)  $R''_f$  obtained by fitting Eq. 14 and Eq. 15.

In general, with increasing  $\phi$ , the hydrodynamic effects represented by the  $A_f$  values increase, with the effect being strongly dependent the GNP SSA (Figure 11A) suggesting enhanced polymer-filler interactions in GNPs with higher SSA. The increase in the  $R'_f$  values with SSA indicates higher elastic contribution, due to the strengthening of the filler network. At low SSAs, the filler network is mediated by the bridging of the polymer chains between filler particles [Chen *et al.* (2015)], whereas at higher SSAs the stress bearing mechanism transitions to a direct particle-particle network. This was also discussed in section III.D with respect to the critical exponent  $b$  of the rheological percolation model. The decrease in  $n_3$  and the increase

in the viscous contributions of the filler phase denoted by  $R''_f$  with GNP SSA suggests a larger interaction zone made up of adsorbed/confined polymer between the interacting GNP tactoids and aggregates.

#### H. Correlation between rheological properties and SSA

One of the objectives of this research was to identify suitable parameters or rheological indicators that have strong correlation with the SSA of the GNPs. Based on the results presented up to now, we propose that the rheological signatures such as  $|\eta^*|_{0.1\text{rad/s}}$ ,  $G'_{0.1\text{rad/s}}$ , yield stress, and the two-phase model parameters, obtained at modest to high  $\phi$ , correlate well with the SSA values. To further demonstrate this concept, intermediate samples were collected at various time intervals during the TME process conducted at 35 N.m [Mardlin *et al.* (2022a)]. As time progresses the graphite particles are delaminated and fragmented by the shear forces and the SSA increases. Figure 12 and S11(A-B) show the evolution of rheology in terms of the complex viscosity, storage modulus and the van Gorp-Palmen plots respectively for intermediate samples of GNP in PEO at 21 wt.%, which was chosen as a value above the percolation threshold. Consistent with the results demonstrated previously, the increase in SSA during the delamination process of graphite translates into enhanced rheological response of the material as can be seen in the  $|\eta^*|$ ,  $G'$  and  $\delta$  frequency sweeps. For the first two samples, GNP64 and GNP100, where the number refers to the SSA of the intermediate, the rheology does not differ compared to the initial graphite sample, within statistical error. In these samples, the increase in SSA is associated with the fragmentation of graphite into smaller sized particles, without considerable exfoliation occurring [Mardlin *et al.* (2022a)]. As the graphite is exfoliated into GNPs, the aspect ratios of fillers increase along with the contact sites for interaction with the matrix and neighbouring particles, which results in noticeable increases in all the melt rheological properties as seen in Figure 12 and S11. These results demonstrate that SAOS characterization can successfully track the exfoliation of graphite into GNPs.

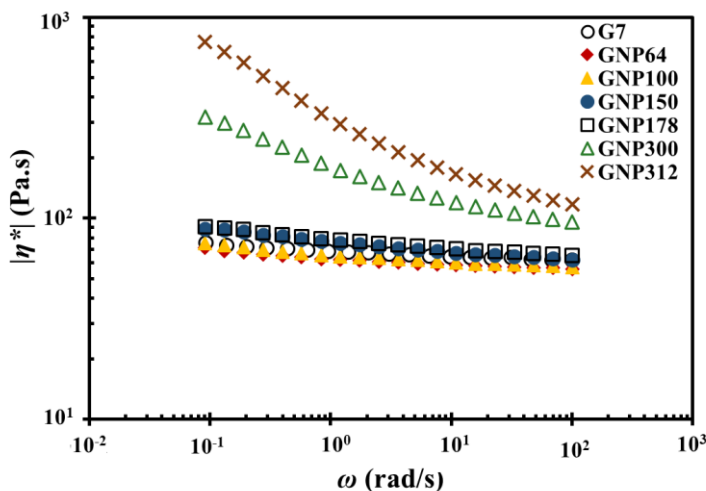


**FIG. 12.** Evolution of complex viscosity for composites containing 21wt.% intermediate GNP samples obtained during the TME process. The number refers to the SSA of the intermediates, which increases as the graphite (G7) is exfoliated for longer times.

In the figures below we combine the findings from the previous sections (noted using closed circles) with the analysis obtained from the intermediates (noted using open symbols). As seen in Figures 13 and S12, all parameters follow a similar coherent trend with increasing filler SSA. First we look at the yield stress. Vergnes (2011) reported that the melt yield stress was an appropriate metric to quantify filler exfoliation level as opposed to the commonly used metrics of zero shear viscosity or power law slope. The yield stress values follow a linear increase up to SSA of 178 m<sup>2</sup>/g as seen in Figure 13(A), beyond which they increase exponentially with SSA.

It is apparent that GNP composites with SSA < 200 m<sup>2</sup>/g have very small yield stress values, lower than 1 Pa. Beyond 200 m<sup>2</sup>/g the yield stress increases exponentially, as shown in Figure 13(A). Following a similar trend, the complex viscosity  $|\eta^*|_{0.1\text{rad/s}}$  (Figure S12A) and storage modulus  $G'_{0.1\text{rad/s}}$  at the lowest measured frequency (Figure S12B), and the two-phase model parameter  $A_f$  (Figure 13A inset) increase exponentially above the SSA of 200 m<sup>2</sup>/g, revealing that the increase in surface area has a significant effect on the polymer/filler and filler/filler interactions. The elastic contribution of the filler phase,  $R'_f$  and the viscous

contribution,  $R''_f$  correlate well with SSA according to the scaling relation shown in Figures 13(B). This demonstrates the sensitivity of the two-phase model parameters as a predictive tool.

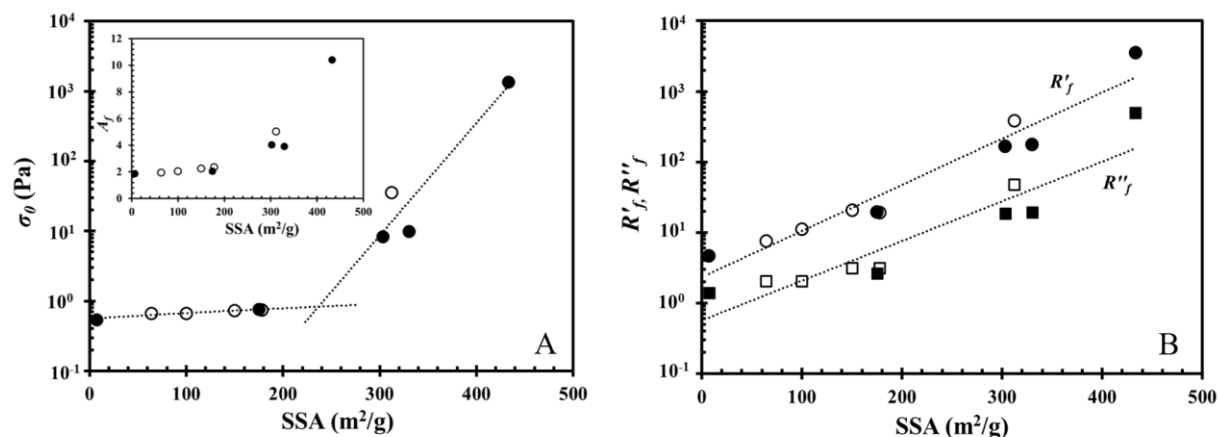


**FIG. 13.** Effect of GNP SSA on rheological parameters A) yield stress  $\sigma_0$  (inset shows two-phase model parameter  $A_f$ ) with the scaling relation obtained from the exponential fitting above SSA of  $200 \text{ m}^2/\text{g}$  found to be  $\sigma_0=10^{-4} \times e^{0.037\text{SSA}}$  and B)  $R'_f$  and  $R''_f$ , where  $R'_f=2.3 \times e^{0.015\text{SSA}}$  and  $R''_f=0.565 \times e^{0.013\text{SSA}}$ . Open circles represent the intermediate samples and the closed circles represent the GNPs discussed in the previous sections.

#### J. Limits of linear viscoelastic region

The strain sweep measurements performed to determine the LVE region for the graphite and GNP composites are shown in Figure 14 and S13 and the critical strain  $\gamma_c$ , defined as the % strain at which  $G'$  reaches 90% of its low-strain value was determined. These values are reported in Table S4.  $\gamma_c$  decreases with increase in  $\phi$  as previously reported for several filled polymer systems [Aranguren *et al.* (1992), Bailly *et al.* (2010), Sabzi *et al.* (2013), Zohrevand *et al.* (2014)].  $\gamma_c$  shows a gradual decrease below the rheological percolation threshold, whereas it decreases dramatically above  $\phi_{per}$  as shown in Figure S14. An interesting observation in the strain sweeps particularly for graphite and GNP175 composites is the appearance of an intermediate strain softening regime accompanied by a two-stage yielding process as well as the occurrence of strain hardening ( $G'$  shows a maximum) at the second yield strain for high  $\phi$  (strain sweep plots for 27 wt.% intermediate samples are shown in Figure S15). Anderson and Zukoski (2009) attributed the presence

of two yield strains to secondary entanglements (entanglements between adsorbed polymer on two neighbouring surfaces and non-adsorbed polymer) in nano silica filled PEO, whereas the origin of strain hardening was attributed to the ordering of entangled polymer segments when confinement effects come into play. In the present case, the phenomenon appears to be more pronounced in graphite, and GNPs having lower SSAs (see also Figure S13 and S15).

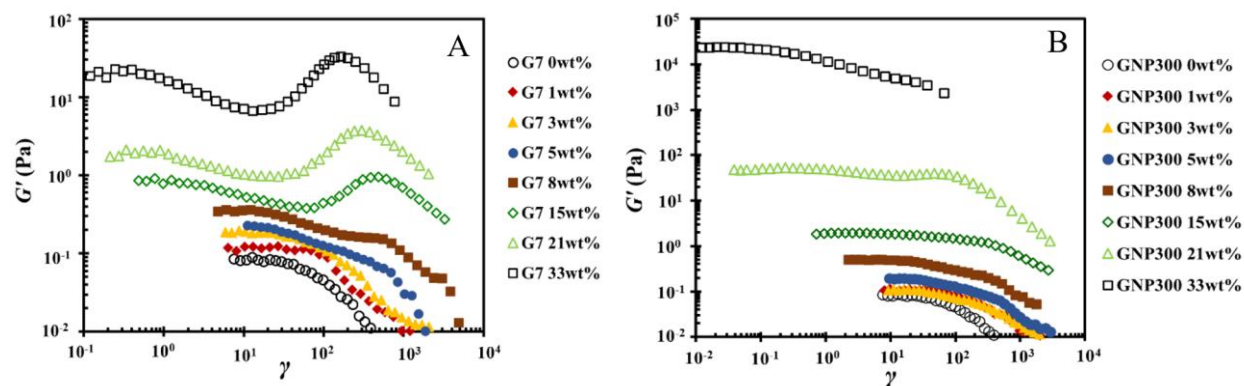


**FIG. 14.** Strain sweep plots showing elastic modulus  $G'$  versus percent strain amplitude  $\gamma$  for A) graphite and B) GNP300 composites. All measurements were performed at 70 °C and at a frequency of 0.1 Hz.

#### J. Fractal gel model

The fractal gel model proposed by Shih *et al.* (1990) has been used to describe quantitatively the aggregate network structure formed in nanocomposites [Vermant *et al.* (2007), Filippone *et al.* (2014), Bossler (2017), Sabzi *et al.* (2013)]. Shih *et al.* (1990) debated that the particle network consisted of several aggregates/flocs of fractal dimension  $d_f$  that are bound together elastically, with the elasticity of the aggregate backbone (where  $x$  is the dimension of the floc backbone) dictating the elastic behaviour of the aggregate filler network. When the interfloc links are stronger than the intrafloc links, the elasticity of the macroscopic gel is governed by the intralinks and this is called the “strong-link regime”. Conversely, when the intrafloc links are stronger than the interfloc links in the “weak-link regime” the gel elasticity is governed by the elasticity of the interfloc links. Shih’s model may lead to non realistic values for  $x$  when applied to polymer/clay and polymer/GNP nanocomposites [Vermant *et al.* (2007), Sabzi *et al.* (2013)]. The modified model proposed by Wu and Morbidelli (2001) accounts for the presence of a transition regime by

introducing a parameter  $\alpha$ , where both inter- and intrafloc links govern the gel elasticity [Filippone *et al.* (2014)]. The scaling relations proposed by the Wu and Morbidelli model are as follows:

$$G'_0 \sim \phi^{\beta/(3-d_f)} \quad (16)$$

$$\gamma_c \sim \phi^{(3-\beta-1)/(3-d_f)} \quad (17)$$

where  $\beta = 1 + (2 + x)(1 - \alpha)$  and denotes relative strength of inter- and interfloc connections in the network [Bossler (2017)],  $G'_0$  is the storage modulus at the lowest measured frequency,  $\gamma_c$  is the critical strain,  $\phi$  is the filler volume fraction.  $\alpha$  ranges between 0 (strong-link regime) to 1 (weak-link regime), with  $0 < \alpha < 1$  indicating the transition regime.

Above the percolation threshold,  $G'_0$  and  $\gamma_c$  scale with the volume fraction  $\phi$ , according to  $G'_0 \sim \phi^s$  and  $\gamma_c \sim \phi^t$  respectively, as shown in Figures 15 (A-B). We can see that the  $s$  and  $t$  values increase as a function of the SSA. Chatterjee and Krishnamoorti (2007) proposed that  $s$  values are governed by the floc-floc interactions either through polymer bridges (mediated) or directly between the filler phase flocs. The higher scaling exponent  $s$  for GNPs with higher SSA could indicate a larger number of inter-floc connections in the percolated network. Upon reaching critical strains, these connections between neighbouring flocs get disrupted and the materials begin to yield/ loose their linear viscoelastic response [Sabzi *et al.* (2013)]. On the other hand,  $t$  values represent the sensitivity of the filled polymer melt to changing strain amplitude [Vermant *et al.* (2007), Zohrevand *et al.* (2014)]. Therefore, increasing  $t$  values reveal that strain sensitivity of the composites increases with filler SSA.

We equate the  $s$  and  $t$  values obtained for graphite and GNP composites with the respective exponents of the fractal gel model given in Eqs. 16 and 17. Taking into account the tortuosity of the network [Filippone *et al.* (2014)], according to which the backbone fractal dimension,  $x$  ranges between 1-1.3 for percolated systems, we assume  $x = 1.3$ . The parameters obtained by solving these equations are presented in Table VI. The  $\alpha$  values suggest that all systems belong to the transition regime.  $d_f$  values range from 2.3 to 2.8 which

are in the same range of values of obtained by Sabzi *et al.* (2013), and Vermant *et al.* (2007) for composites containing GNPs ( $d_f = 2.2$  and  $2.4$ ) and nanoclays ( $d_f = 2.2$  and  $2.4$ ) respectively. The higher  $\beta$  values tending towards the limiting case of  $\beta \sim 4.3$  for the strong-link regime suggest that the interfloc links are stronger than the intra floc links in these systems that contain loosely aggregated particles.

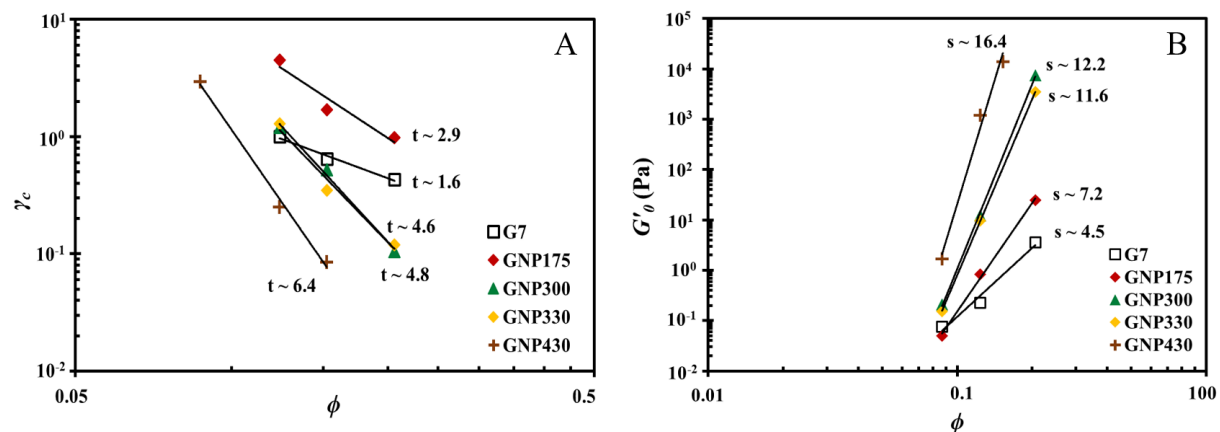


**FIG. 15.** A)  $\gamma_c$  and B)  $G'$  versus  $\phi$  as a function of GNP SSA at high concentrations.

Cassagnau (2008) warns that the accurate experimental determination of the exponents used in Eqs. 16 and 17 is difficult and therefore the possibilities of error must be kept in mind while using these determinations to directly quantify degree of exfoliation. For verification of  $d_f$  values obtained from these empirical models SAXS can be a useful technique in future work, as demonstrated by Baeza *et al.* (2013) for nanocomposite silica/SBR systems.

**Table VI.** Values of  $d_f$ ,  $\beta$  and  $\alpha$  determined from Eq. 16 and 17, assuming  $x = 1.3$ .

	$d_f$	$\beta$	$\alpha$
Graphite	2.3	3.1	0.4
GNP175	2.5	3.4	0.3
GNP300	2.7	3.3	0.3
GNP330	2.8	2.8	0.5
GNP430	2.8	3.3	0.3

#### IV. CONCLUSIONS

We used a series of well-characterized GNPs having varying SSAs, which were produced from graphite in a controlled manner using a newly developed TME process, to study the effect of filler SSA on the rheological properties of PEO/GNP composites. We verified the liquid-to-solid transition brought about by the formation of the electrically conducting, space-filling filler network by examining the van Gorp-Palmen plots and the appearance of yield stresses. The electrical and rheological percolation thresholds,  $\phi_c$  and  $\phi_{per}$  respectively, decreased with increasing filler SSA, with  $\phi_c$  ranging from 10.4 to 8.1 vol.% and  $\phi_{per}$  ranging from 12.4 to 5.4 vol.% for graphite to GNP430 composites.

The TEM images for graphite and GNP composites at low filler concentrations showed isolated, individual platelets whereas at high filler concentrations they were aggregated into larger tactoids. We used the models proposed by Utracki and Lyngaae-Jørgensen (2002) and Krieger and Daugherty [Beuguel *et al.* (2018)] to fit the reduced viscosity as a function of filler loading at low and high filler concentrations respectively. In the non-interacting regime, the filler aspect ratio, defined as length/thickness ranged between 19 for the lowest SSA to 76 for the higher SSA. In the interacting regime, the aspect ratio was defined as the length/width of the tactoids/aggregates and ranged between 5-24.

The two-phase model revealed that the composite melt viscosity was governed by hydrodynamic effects up to filler contents of 8 wt.%. Above this, as interparticle distances decreased, filler-filler interactions, governed by direct contact between the filler domains, or mediated by polymer bridging played a significant role in increasing the elasticity of the network. We demonstrated scaling relationships for the yield stress, the two-phase model parameters, and the critical strain with the SSAs of the GNPs. The fractal gel model was used in conjunction with stress sweep measurements to estimate the fractal dimensions of the aggregates, which ranged from 2.3 to 2.8.

Using intermediate GNP samples having various SSAs, we demonstrated that various rheological signatures can be used to successfully track the exfoliation of graphite into GNPs. The ability to correlate

This is the author's peer reviewed, accepted manuscript. However, the online version of record will be different from this version once it has been copyedited and typeset.  
PLEASE CITE THIS ARTICLE AS DOI: 10.1122/1.50000531

key rheological signatures to the SSA of the GNPs demonstrates that rheology can serve as a valuable bulk characterization method for these systems.

### **Supplementary material**

See supplementary material for the model equations, image analysis, rheological characterization of all composites and the model fits.

### **Acknowledgments**

Financial support from the Natural Sciences and Engineering Research Council of Canada (NSERC), and a Queen's Graduate Award from Queen's University is gratefully acknowledged. The authors would like to thank Kent Mardlin for producing the GNPs and Dr. Quang Binh Ho for the sample preparation for contact angle measurements.

## References

- Abbasi, S., Carreau, P. J., Derdouri, A., and Moan, M., “Rheological properties and percolation in suspensions of multiwalled carbon nanotubes in polycarbonate,” *Rheologica Acta* 48, 943-959 (2009).
- Abdel-Goad, M., Pötschke, P., Zhou, D., Mark, J. E., and Heinrich, G., “Preparation and Rheological Characterization of Polymer Nanocomposites Based on Expanded Graphite,” *Journal of Macromolecular Science, Part A* 44, 591-598 (2007).
- Akpan, E., Shen, X., Wetzel, B., and Friedrich, K., “Design and synthesis of polymer nanocomposites.” *Polymer Composites with Functionalized Nanoparticles* (Elsevier, 2019).
- Anderson, B. J., and Zukoski, C. F., “Rheology and Microstructure of Entangled Polymer Nanocomposite Melts,” *Macromolecules* 42, 8370-8384 (2009).
- Aoyama, S., Ismail, I., Park, Y. T., Macosko, C. W., and Ougizawa, T., “PET/Graphene Compatibilization for Different Aspect Ratio Graphenes via Trimellitic Anhydride Functionalization,” *ACS Omega* 5, 3228-3239 (2020).
- Aram, E., Ehsani, M., Khonakdar, H. A., Jafari, S. H., and Nouri, N. R., “Functionalization of graphene nanosheets and its dispersion in PMMA/PEO blend: Thermal, electrical, morphological and rheological analyses,” *Fibers and Polymers* 17, 174-180 (2016).
- Aranguren, M. I., Mora, E., DeGroot, J. V., and Macosko, C. W., “Effect of reinforcing fillers on the rheology of polymer melts,” *Journal of Rheology* 36, 1165-1182 (1992).
- Baeza, G. P., Dessi, C., Costanzo, S., Zhao, D., Gong, S., Alegria, A., Colby, R. H., Rubinstein, M., Vlassopoulos, D., and Kumar, S. K., “Network dynamics in nanofilled polymers,” *Nature communications* 7, 1-6 (2016).
- Baeza, G. P., Genix, A.-C., Degrandcourt, C., Petitjean, L., Gummel, J., Couty, M., and Oberdisse, J., “Multiscale filler structure in simplified industrial nanocomposite silica/SBR systems studied by SAXS and TEM,” *Macromolecules* 46, 317-329 (2013).

Baeza, G. P., Oberdisse, J., Alegria, A., Couty, M., and Genix, A.-C., “A high-temperature dielectric process as a probe of large-scale silica filler structure in simplified industrial nanocomposites,” *Physical Chemistry Chemical Physics* 17, 1660-1666 (2015).

Bailly, M., and Kontopoulou, M., “Linear viscoelastic properties of ethylene–octene copolymer/nanosilica composites investigated over a broad range of frequencies,” *Journal of Rheology* 57, 407-426 (2013).

Bailly, M., Kontopoulou, M., and El Mabrouk, K., “Effect of polymer/filler interactions on the structure and rheological properties of ethylene-octene copolymer/nanosilica composites,” *Polymer* 51, 5506-5515 (2010).

Baptista, R., Mendão, A., Rodrigues, F., Figueiredo-Pina, C. G., Guedes, M., and Marat-Mendes, R., “Effect of high graphite filler contents on the mechanical and tribological failure behavior of epoxy matrix composites,” *Theoretical and Applied Fracture Mechanics* 85, 113-124 (2016).

Barnes, H. A., “A review of the rheology of filled viscoelastic systems,” *Rheology reviews*, 1-36 (2003).

Barwich, S., Coleman, J. N., and Mobius, M. E., “Yielding and flow of highly concentrated, few-layer graphene suspensions,” *Soft Matter* 11, 3159-64 (2015).

Becker, O., Sopade, P., Bourdonnay, R., Halley, P. J., and Simon, G. P., “Layered silicate nanocomposites based on various high-functionality epoxy resins. Part II: The influence of an organoclay on the rheological behavior of epoxy prepolymers,” *Polymer Engineering & Science* 43, 1683-1690 (2003).

Beuguel, Q., Mija, A., Vergnes, B., and Peuvrel-Disdier, E., “Structural, thermal, rheological and mechanical properties of polypropylene/graphene nanoplatelets composites: Effect of particle size and melt mixing conditions,” *Polymer Engineering & Science* 58, 1937-1944 (2018).

Bhattacharyya, A. R., Sreekumar, T., Liu, T., Kumar, S., Ericson, L. M., Hauge, R. H., and Smalley, R. E., “Crystallization and orientation studies in polypropylene/single wall carbon nanotube composite,” *Polymer* 44, 2373-2377 (2003).

Bossler, F., Maurath, J., Dyhr, K., Willenbacher, N., and Koos, E., “Fractal approaches to characterize the structure of capillary suspensions using rheology and confocal microscopy,” *Journal of rheology* 62, 183-196 (2018).

- Buzaglo, M., Ruse, E., Levy, I., Nadiv, R., Reuveni, G., Shtein, M., and Regev, O., “Top-down, scalable graphene sheets production: It is all about the precipitate,” *Chemistry of Materials* 29, 9998-10006 (2017).
- Canales, J., Muñoz, M. E., Fernández, M., and Santamaría, A., “Rheology, electrical conductivity and crystallinity of a polyurethane/graphene composite: Implications for its use as a hot-melt adhesive,” *Composites Part A: Applied Science and Manufacturing* 84, 9-16 (2016).
- Carotenuto, C., Rexha, G., Martone, R., and Minale, M., “The microstructural change causing the failure of the Cox-Merz rule in Newtonian suspensions: Experiments and simulations,” *Rheologica Acta* 60, 309-325 (2021).
- Cassagnau, P., “Melt rheology of organoclay and fumed silica nanocomposites,” *Polymer* 49, 2183-2196 (2008).
- Chatterjee, T., and Krishnamoorti, R., “Dynamic consequences of the fractal network of nanotube-poly(ethylene oxide) nanocomposites,” *Physical Review E* 75 (2007).
- Chen, Q., Gong, S., Moll, J., Zhao, D., Kumar, S. K., and Colby, R. H., “Mechanical reinforcement of polymer nanocomposites from percolation of a nanoparticle network, ” *ACS Macro Letters* 4,398-402 (2015).
- Claypole, A., Claypole, J., Claypole, T., Gethin, D., and Kilduff, L., “The effect of plasma functionalization on the print performance and time stability of graphite nanoplatelet electrically conducting inks,” *Journal of Coatings Technology and Research* 18, 193-203 (2020).
- El Achaby, M., Arrakhiz, F.-E., Vaudreuil, S., el Kacem Qaiss, A., Bousmina, M., and Fassi-Fehri, O., “Mechanical, thermal, and rheological properties of graphene-based polypropylene nanocomposites prepared by melt mixing,” *Polymer Composites* 33, 733-744 (2012).
- Eslami, H., Grmela, M., and Bousmina, M., “Linear and nonlinear rheology of polymer/layered silicate nanocomposites,” *Journal of Rheology* 54, 539-562 (2010).
- Ferreira, W. H., Dahmouche, K., and Andrade, C. T., “Dispersion of reduced graphene oxide within thermoplastic starch/poly (lactic acid) blends investigated by small-angle X-ray scattering,” *Carbohydrate polymers* 208, 124-132 (2019).

This is the author's peer reviewed, accepted manuscript. However, the online version of record will be different from this version once it has been copyedited and typeset.  
PLEASE CITE THIS ARTICLE AS DOI: 10.1122/1.5111111

Fetters, L., Lohse, D., and Colby, R., “Chain dimensions and entanglement spacings.” Physical properties of polymers handbook, Springer New York (2007).

Filippone, G., Causa, A., de Luna, M. S., Sanguigno, L., and Acierno, D., “Assembly of plate-like nanoparticles in immiscible polymer blends—effect of the presence of a preferred liquid–liquid interface,” *Soft Matter* 10, 3183-3191 (2014).

Gantenbein, D., Schoelkopf, J., Matthews, G. P., and Gane, P. A., “Determining the size distribution-defined aspect ratio of rod-like particles,” *Applied clay science* 53, 538-543 (2011).

Gao, C., Liu, P., Ding, Y., Li, T., Wang, F., Chen, J., Zhang, S., Li, Z., and Yang, M., “Non-contact percolation of unstable graphene networks in poly (styrene-co-acrylonitrile) nanocomposites: Electrical and rheological properties,” *Composites Science and Technology* 155, 41-49 (2018).

Ghanbari, A., Heuzey, M. C., Carreau, P. J., and Ton-That, M. T., “Morphological and rheological properties of PET/clay nanocomposites,” *Rheologica Acta* 52, 59-74 (2013).

Graziano, F., Cohen, R., and Medalia, A., “Rheology of concentrated suspensions of carbon black in low molecular weight vehicles,” *Rheologica Acta* 18, 640-656 (1979).

Guth, E., and Gold, O., “On the hydrodynamical theory of the viscosity of suspensions,” *Physics Review* 53, 322-322 (1938).

Hadaeghnia, M., Ahmadi, S., Ghasemi, I., and Wood-Adams, P. M., “Manipulating the morphology of PA6/POE blends using graphene to achieve balanced electrical and mechanical properties,” *Composites Science and Technology* 200, 108412 (2020).

He, S., Zhang, J., Xiao, X., Hong, X., and Lai, Y., “Investigation of the conductive network formation of polypropylene/graphene nanoplatelets composites for different platelet sizes,” *Journal of Materials Science* 52, 13103-13119 (2017).

Helal, E., Kurusu, R. S., Moghimian, N., Gutierrez, G., David, E., and Demarquette, N. R., “Correlation between morphology, rheological behavior, and electrical behavior of conductive cocontinuous

This is the author's peer reviewed, accepted manuscript. However, the online version of record will be different from this version once it has been copyedited and typeset.  
PLEASE CITE THIS ARTICLE AS DOI: 10.1122/1.511111

LLDPE/EVA blends containing commercial graphene nanoplatelets,” *Journal of Rheology* 63, 961-976 (2019).

Hernandez, Y., Nicolosi, V., Lotya, M., Blighe, F. M., Sun, Z., De, S., McGovern, I. T., Holland, B., Byrne, M., Gun'Ko, Y. K., Boland, J. J., Niraj, P., Duesberg, G., Krishnamurthy, S., Goodhue, R., Hutchison, J., Scardaci, V., Ferrari, A. C., and Coleman, J. N., “High-yield production of graphene by liquid-phase exfoliation of graphite,” *Nat Nanotechnol* 3, 563-8 (2008).

Ho, Q. B., and Kontopoulou, M., “Stabilization of the cellular structure of polypropylene foams and secondary nucleation mechanism in the presence of graphene nanoplatelets,” *Polymer* 198 (2020).

Ho, Q. B., and Kontopoulou, M., “Compatibilized polypropylene nanocomposites containing expanded graphite and graphene nanoplatelets,” *Polymer Engineering & Science* 61, 1116-1128 (2021).

Ho, Q. B., Osazuwa, O., Modler, R., Daymond, M., Gallerneault, M. T., and Kontopoulou, M., “Exfoliation of graphite and expanded graphite by melt compounding to prepare reinforced, thermally and electrically conducting polyamide composites,” *Composites Science and Technology* 176, 111-120 (2019).

Iqbal, M. Z., Abdala, A. A., Mittal, V., Seifert, S., Herring, A. M., and Liberatore, M. W., “Processable conductive graphene/polyethylene nanocomposites: Effects of graphene dispersion and polyethylene blending with oxidized polyethylene on rheology and microstructure,” *Polymer* 98, 143-155 (2016).

Joseph, R., McGregor, W., Martyn, M., Tanner, K., and Coates, P., “Effect of hydroxyapatite morphology/surface area on the rheology and processability of hydroxyapatite filled polyethylene composites,” *Biomaterials* 23, 4295-4302 (2002).

Kalaitzidou, K., Fukushima, H., and Drzal, L. T., “Multifunctional polypropylene composites produced by incorporation of exfoliated graphite nanoplatelets,” *Carbon* 45, 1446-1452 (2007).

Kashi, S., Gupta, R. K., Baum, T., Kao, N., and Bhattacharya, S. N., “Phase transition and anomalous rheological behaviour of polylactide/graphene nanocomposites,” *Composites Part B: Engineering* 135, 25-34 (2018).

This is the author's peer reviewed, accepted manuscript. However, the online version of record will be different from this version once it has been copyedited and typeset.  
PLEASE CITE THIS ARTICLE AS DOI: 10.1122/1.5111111

Kauly, T., Siegmund, A., and Shacham, D., “Rheology of highly filled natural CaCO<sub>3</sub> composites. II. Effects of solid loading and particle size distribution on rotational rheometry,” *Polymer composites* 28, 524-533 (2007).

Kazemi-Khasragh, E., Bahari-Sambran, F., Platzer, C., and Eslami-Farsani, R., “The synergistic effect of graphene nanoplatelets–montmorillonite hybrid system on tribological behavior of epoxy-based nanocomposites,” *Tribology International* 151, 106472 (2020).

Khalkhal, F., Carreau, P. J., and Ausias, G., “Effect of flow history on linear viscoelastic properties and the evolution of the structure of multiwalled carbon nanotube suspensions in an epoxy,” *Journal of Rheology* 55, 153-175 (2011).

Kim, H. B., Lee, C. H., Choi, J. S., Park, B. J., Lim, S. T., and Choi, H. J., “Preparation and rheological characteristics of poly (ε-caprolactone)/organoclay nanocomposites,” *Journal of Industrial and Engineering Chemistry* 11, 769-772 (2005).

King, J. A., Via, M. D., Morrison, F. A., Wiese, K. R., Beach, E. A., Cieslinski, M. J., and Bogucki, G. R., “Characterization of exfoliated graphite nanoplatelets/polycarbonate composites: electrical and thermal conductivity, and tensile, flexural, and rheological properties,” *Journal of Composite Materials* 46, 1029-1039 (2011).

Kong, W., Kum, H., Bae, S.-H., Shim, J., Kim, H., Kong, L., Meng, Y., Wang, K., Kim, C., and Kim, J., “Path towards graphene commercialization from lab to market,” *Nature nanotechnology* 14, 927-938 (2019).

Kota, A. K., Cipriano, B. H., Dueterberg, M. K., Gershon, A. L., Powell, D., Raghavan, S. R., and Bruck, H. A., “Electrical and rheological percolation in polystyrene/MWCNT nanocomposites,” *Macromolecules* 40, 7400-7406 (2007).

Kotsilkova, R., Tabakova, S., and Ivanova, R., “Effect of graphene nanoplatelets and multiwalled carbon nanotubes on the viscous and viscoelastic properties and printability of polylactide nanocomposites,” *Mechanics of Time-Dependent Materials* (2021).

Krishnamoorti, R., and Yurekli, K., “Rheology of polymer layered silicate nanocomposites,” *Current Opinion in Colloid & Interface Science* 6, 464-470 (2001).

Li, B., Guo, Y., Steeman, P., Bulters, M., and Yu, W., “Shear-induced breakdown and agglomeration in nanoparticles filled polymer: The shift of phase boundary and kinetics,” *Journal of Rheology* 65, 291-309 (2021).

Li, D., Müller, M. B., Gilje, S., Kaner, R. B., and Wallace, G. G., “Processable aqueous dispersions of graphene nanosheets,” *Nature nanotechnology* 3, 101-105 (2008).

Li, Y., Zhu, J., Wei, S., Ryu, J., Sun, L., and Guo, Z., “Poly(propylene)/Graphene Nanoplatelet Nanocomposites: Melt Rheological Behavior and Thermal, Electrical, and Electronic Properties,” *Macromolecular Chemistry and Physics* 212, 1951-1959 (2011).

Lin, L., Peng, H., and Liu, Z., “Synthesis challenges for graphene industry,” *Nature materials* 18, 520-524 (2019).

Mardlin, K., Osazuwa, O., and Kontopoulou, M., “Solvent-Free Thermomechanical Exfoliation of Graphite into Graphene Nanoplatelet Flakes: Implications for Conductive Composites,” *ACS Applied Nano Materials* 5, 4938-4947 (2022a).

Mardlin, K., Osazuwa, O., Kontopoulou, M., and Leelapornpisit, W., “Polyamide composites containing graphene nanoplatelets produced via thermomechanical exfoliation,” *Composites Science and Technology* 225, 109493 (2022b).

Mayoral, B., Harkin-Jones, E., Khanam, P. N., AlMaadeed, M. A., Ouederni, M., Hamilton, A. R., and Sun, D., “Melt processing and characterisation of polyamide 6/graphene nanoplatelet composites,” *RSC Advances* 5, 52395-52409 (2015).

Metzner, A., “Rheology of suspensions in polymeric liquids,” *Journal of rheology* 29, 739-775 (1985).

Mewis, J., and Wagner, N. J., “Thixotropy,” *Advances in colloid and interface science* 147, 214-227 (2009).

- Mohamadi, M., Papila, M., Garmabi, H., and Gohari Bajestani, Z., “Morphological evaluation and phase behavior of PVDF/PEO blends in the presence of graphene nanoplatelets through rheological measurements,” *Journal of Applied Polymer Science* 136 (2019).
- Nazockdast, E., Nazockdast, H., and Goharpey, F., “Linear and nonlinear melt-state viscoelastic properties of polypropylene/organoclay nanocomposites,” *Polymer Engineering & Science* 48, 1240-1249 (2008).
- Nieto, A., Lahiri, D., and Agarwal, A., “Synthesis and properties of bulk graphene nanoplatelets consolidated by spark plasma sintering,” *Carbon* 50, 4068-4077 (2012).
- Nutz, M., Furdin, G., Medjahdi, G., Marêché, J., and Moreau, M., “Rheological properties of coal tar pitches containing micronic graphite powders,” *Carbon* 35, 1023-1029 (1997).
- Osman, M. A., and Atallah, A., “Effect of the particle size on the viscoelastic properties of filled polyethylene,” *Polymer* 47, 2357-2368 (2006).
- Papadopoulou, A., Gillissen, J. J., Tiwari, M. K., and Balabani, S., “Effect of particle specific surface area on the rheology of non-brownian silica suspensions,” *Materials* 13, 4628 (2020).
- Rahmanian, V., and Galeski, A., “Cavitation in strained polyethylene/nanographene nanocomposites,” *Polymer* 232, 124158 (2021).
- Ren, J., Silva, A. S., and Krishnamoorti, R., “Linear viscoelasticity of disordered polystyrene–polyisoprene block copolymer based layered-silicate nanocomposites,” *Macromolecules* 33, 3739-3746 (2000).
- Ren, W., and Cheng, H.-M., “The global growth of graphene,” *Nature nanotechnology* 9, 726-730 (2014).
- Sabzi, M., Jiang, L., Liu, F., Ghasemi, I., and Atai, M., “Graphene nanoplatelets as poly (lactic acid) modifier: linear rheological behavior and electrical conductivity,” *Journal of materials chemistry A* 1, 8253-8261 (2013).
- Ruschau, G., Yoshikawa, S., and Newnham, R., “Resistivities of conductive composites,” *Journal of applied physics* 72, 953-959 (1992).
- Samoilov, V., “Specific surface area, shape, and size of fine carbon filler particles,” *Inorganic Materials* 46, 818-823 (2010).

Sethy, S., Samantara, L., and Satapathy, B. K., “Phase-selective micro-structural effects on rheological-networks, segmental relaxation, and electrical conductivity behavior of melt-mixed polyamide-12/polypropylene-multi walled carbon nanotubes ternary nanocomposites,” *Polymer Engineering & Science* 60, 1301-1315 (2020).

Shafiei-Sabet, S., Hamad, W. Y., and Hatzikiriakos, S. G., “Rheology of nanocrystalline cellulose aqueous suspensions,” *Langmuir* 28, 17124-17133 (2012).

Shih, W.-H., Shih, W. Y., Kim, S.-I., Liu, J., and Aksay, I. A., “Scaling behavior of the elastic properties of colloidal gels,” *Physical review A* 42, 4772-4779 (1990).

Song, Y., and Zheng, Q., “Linear viscoelasticity of polymer melts filled with nano-sized fillers,” *Polymer* 51, 3262-3268 (2010).

Song, Y., and Zheng, Q., “Application of two phase model to linear dynamic rheology of filled polymer melts,” *Polymer* 52, 6173-6179 (2011).

Song, Y., and Zheng, Q., “Linear rheology of nanofilled polymers,” *Journal of Rheology* 59, 155-191 (2015).

Song, Y. S., “Rheological characterization of carbon nanotubes/poly(ethylene oxide) composites,” *Rheologica Acta* 46, 231-238 (2006).

Su, X., Wang, R., Li, X., Araby, S., Kuan, H.-C., Naeem, M., and Ma, J., “A comparative study of polymer nanocomposites containing multi-walled carbon nanotubes and graphene nanoplatelets,” *Nano Materials Science* (2021).

Texter, J., “Graphene dispersions,” *Current Opinion in Colloid & Interface Science* 19, 163-174 (2014).

Utracki, L. A., and Lyngaae-Jørgensen, J., “Dynamic melt flow of nanocomposites based on poly-ε-caprolactam,” *Rheologica acta* 41, 394-407 (2002).

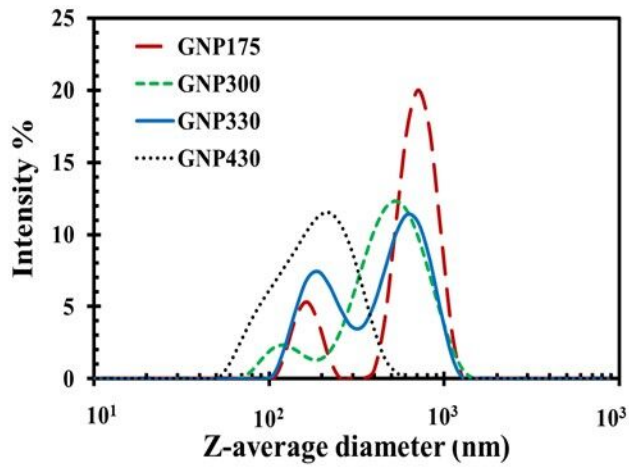
Van Oss, C. J., “Use of the combined Lifshitz–van der Waals and Lewis acid–base approaches in determining the apolar and polar contributions to surface and interfacial tensions and free energies,” *Journal of adhesion science and technology* 16, 669-677 (2002).

- Vasileiou, A. A., Docoslis, A., Kontopoulou, M., Xiang, P., and Ye, Z., “The role of non-covalent interactions and matrix viscosity on the dispersion and properties of LLDPE/MWCNT nanocomposites,” *Polymer* 54, 5230-5240 (2013).
- Vdović, N., Jurina, I., Škapin, S. D., and Sondi, I., “The surface properties of clay minerals modified by intensive dry milling—revisited,” *Applied Clay Science* 48, 575-580 (2010).
- Vergnes, B., “The use of apparent yield stress to characterize exfoliation in polymer nanocomposites,” *International polymer processing* 26, 229-232 (2011).
- Vermant, J., Ceccia, S., Dolgovskij, M. K., Maffettone, P. L., and Macosko, C. W., “Quantifying dispersion of layered nanocomposites via melt rheology,” *Journal of Rheology* 51, 429-450 (2007).
- Wang, J., Guo, Y., Yu, W., Zhou, C., and Steeman, P., “Linear and nonlinear viscoelasticity of polymer/silica nanocomposites: an understanding from modulus decomposition,” *Rheologica Acta* 55, 37-50 (2016).
- Wang, S., Zhang, Y., Abidi, N., and Cabrales, L., “Wettability and surface free energy of graphene films,” *Langmuir* 25, 11078-11081 (2009).
- Wu, D., Wu, L., Zhou, W., Sun, Y., and Zhang, M., “Relations between the aspect ratio of carbon nanotubes and the formation of percolation networks in biodegradable polylactide/carbon nanotube composites,” *Journal of Polymer Science Part B: Polymer Physics* 48, 479-489 (2010).
- Wu, S., “Interfacial energy, structure, and adhesion between polymers,” *Polymer blends*, Academic Press, 243-293 (1978).
- Wu, S., “Polymer interface and adhesion,” Marcel and Dekker Inc. (1982).
- Yang, S.-Y., Lin, W.-N., Huang, Y.-L., Tien, H.-W., Wang, J.-Y., Ma, C.-C. M., Li, S.-M., and Wang, Y.-S., “Synergetic effects of graphene platelets and carbon nanotubes on the mechanical and thermal properties of epoxy composites,” *Carbon* 49, 793-803 (2011).
- Yang, X., Zhan, Y., Zhao, R., and Liu, X., “Effects of graphene nanosheets on the dielectric, mechanical, thermal properties, and rheological behaviors of poly(arylene ether nitriles),” *Journal of Applied Polymer Science* 124, 1723-1730 (2012).

This is the author's peer reviewed, accepted manuscript. However, the online version of record will be different from this version once it has been copyedited and typeset.  
PLEASE CITE THIS ARTICLE AS DOI: 10.1122/1.5000531

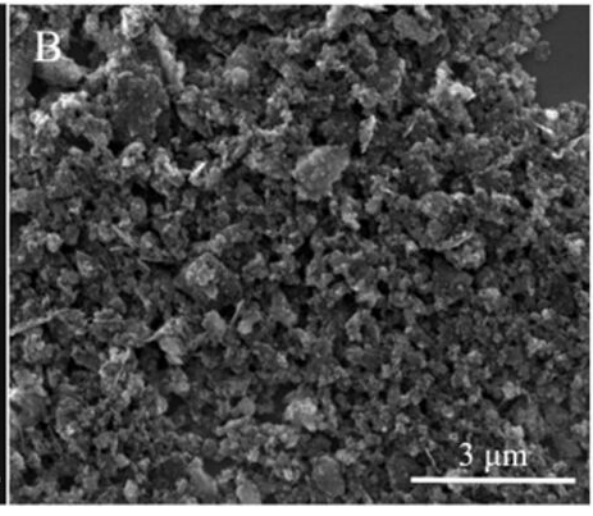
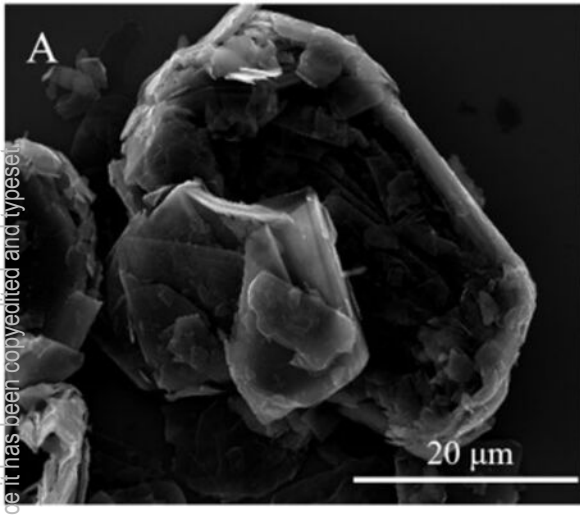
- Yasmin, A., Luo, J.-J., and Daniel, I. M., “Processing of expanded graphite reinforced polymer nanocomposites,” *Composites Science and Technology* 66, 1182-1189 (2006).
- Ye, R., and Tour, J. M., “Graphene at Fifteen,” *ACS Nano* 13, 10872-10878 (2019).
- Yearsley, K. M., Mackley, M. R., Chinesta, F., and Leygue, A., “The rheology of multiwalled carbon nanotube and carbon black suspensions,” *Journal of Rheology* 56, 1465-1490 (2012).
- Yuan, J., and Murray, H. H., “The importance of crystal morphology on the viscosity of concentrated suspensions of kaolins,” *Applied Clay Science* 12, 209-219 (1997).
- Zhang, Q., and Archer, L. A., “Poly (ethylene oxide)/silica nanocomposites: structure and rheology,” *Langmuir* 18, 10435-10442 (2002).
- Zhu, Y. W., Ji, H. X., Cheng, H. M., and Ruoff, R. S., “Mass production and industrial applications of graphene materials,” *National Science Review* 5, 90-101 (2018).
- Zohrevand, A., Ajji, A., and Mighri, F., “Relationship between rheological and electrical percolation in a polymer nanocomposite with semiconductor inclusions,” *Rheologica Acta* 53, 235-254 (2014).
- Zurutuza, A., and Marinelli, C., “Challenges and opportunities in graphene commercialization,” *Nature nanotechnology* 9, 730-734 (2014).

This is the author's peer reviewed, accepted manuscript. However, the online version of record will be different from this version once it has been copyedited and typeset.  
PLEASE CITE THIS ARTICLE AS DOI: 10.1122/8.0000531



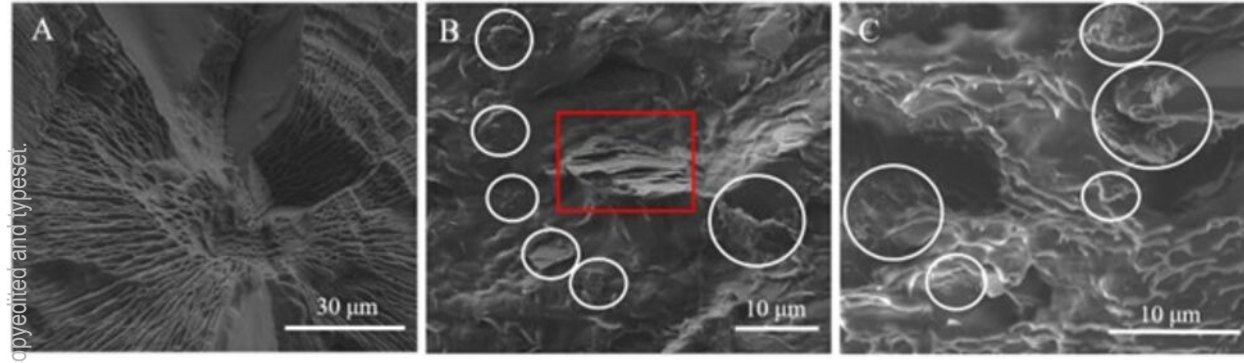
This is the author's peer reviewed, accepted manuscript. However, the online version of record will be different from this version once it has been copyedited and typeset.

PLEASE CITE THIS ARTICLE AS DOI: 10.1122/8.0000531

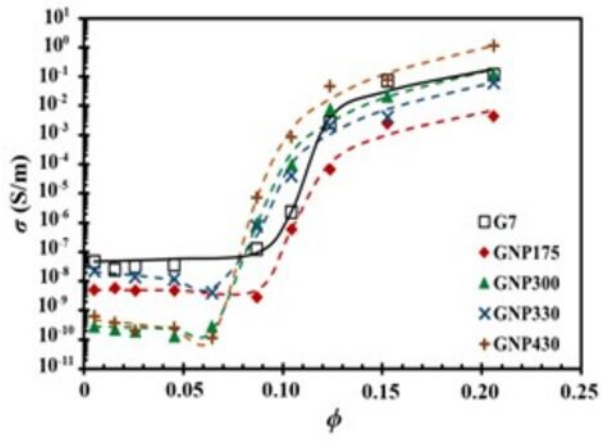


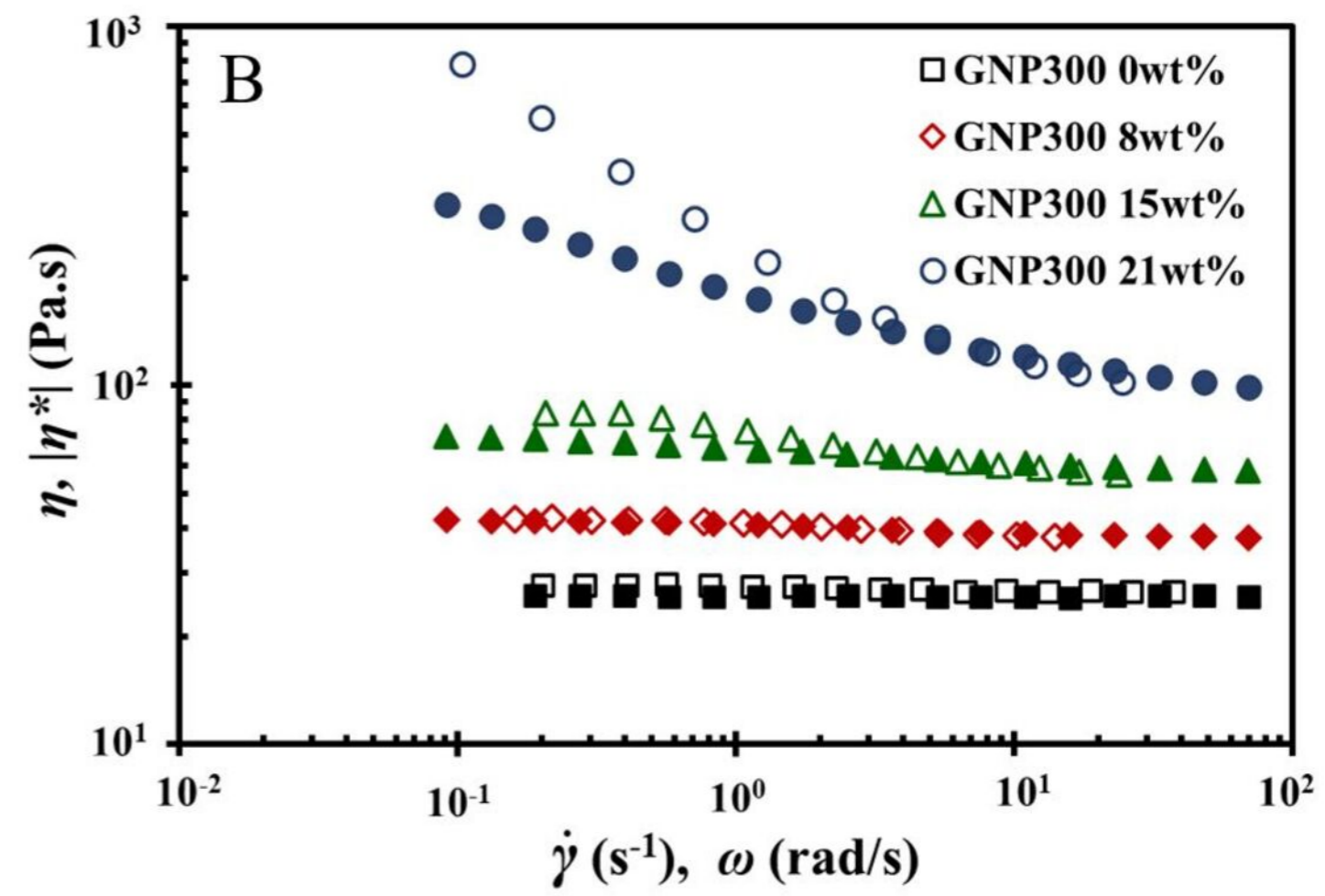
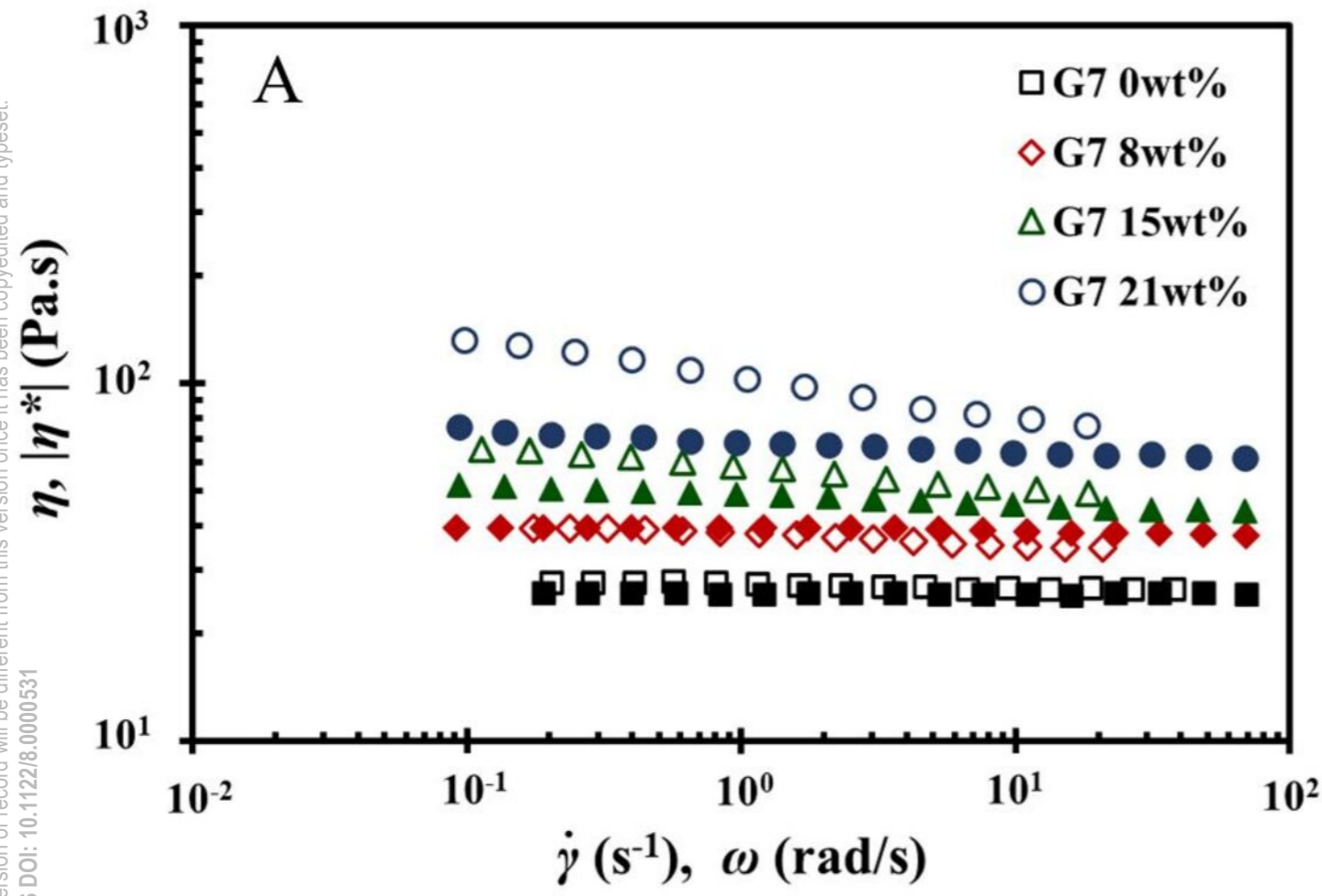
This is the author's peer reviewed, accepted manuscript. However, the online version of record will be different from this version once it has been copyedited and typeset.

PLEASE CITE THIS ARTICLE AS DOI: 10.1122/8.0000531

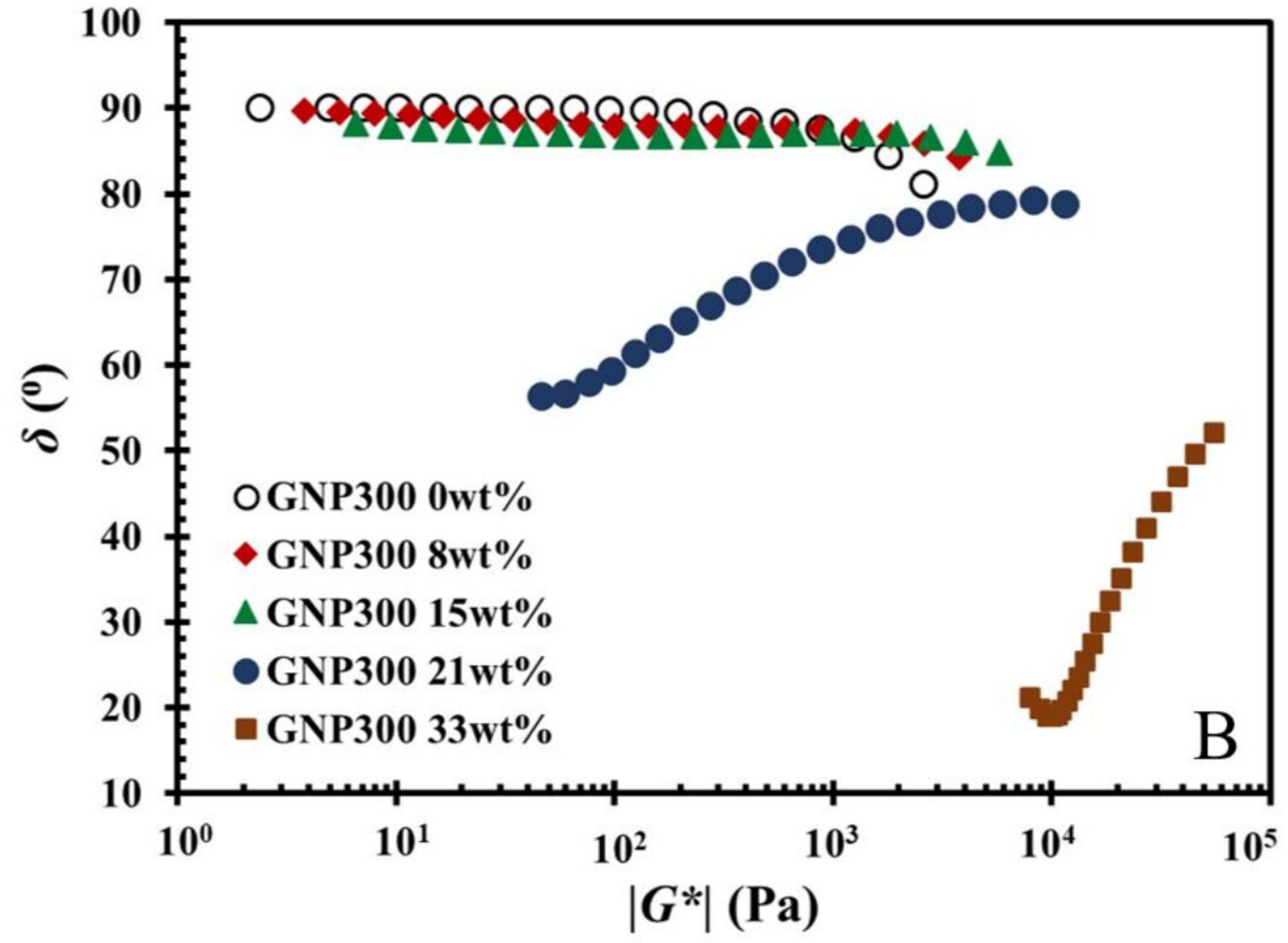
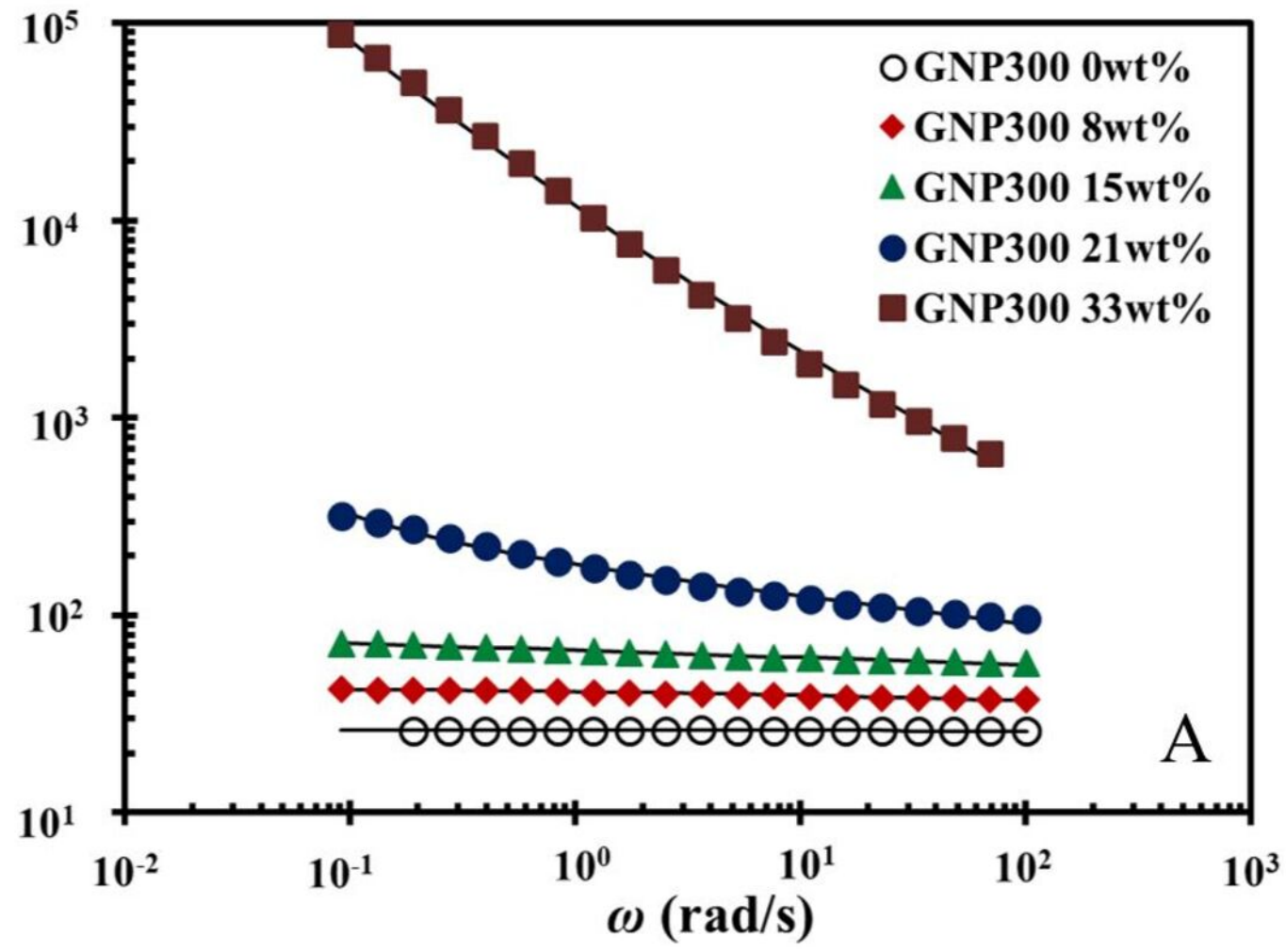


This is the author's peer reviewed, accepted manuscript. However, the online version of record will be different from this version once it has been copyedited and typeset.  
PLEASE CITE THIS ARTICLE AS DOI: 10.1122/8.0000531

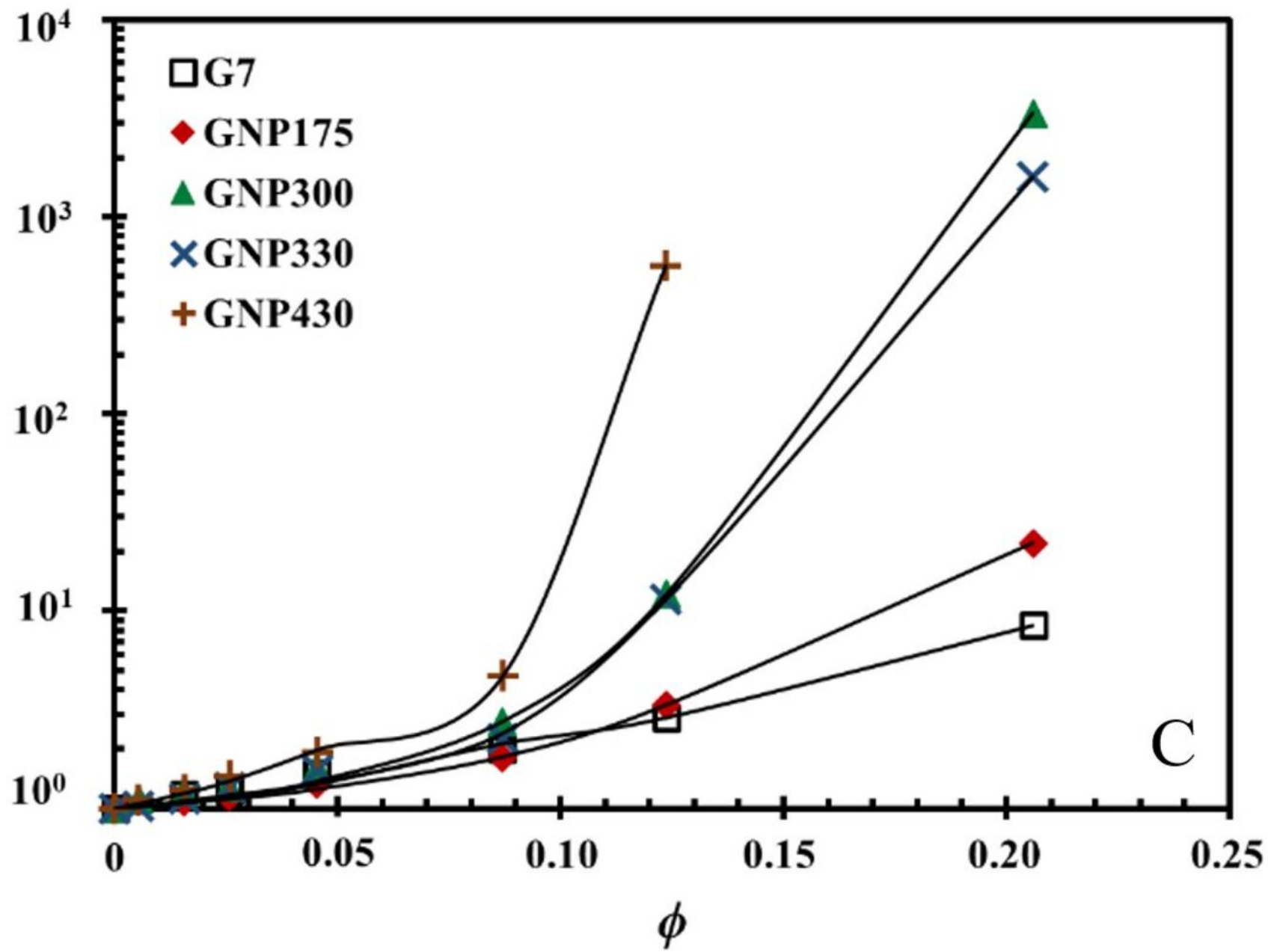




This is the author's peer reviewed, accepted manuscript. However, the online version of record will be different from this version once it has been copyedited and typeset.  
PLEASE CITE THIS ARTICLE AS DOI: 10.1122/1.8.0000531

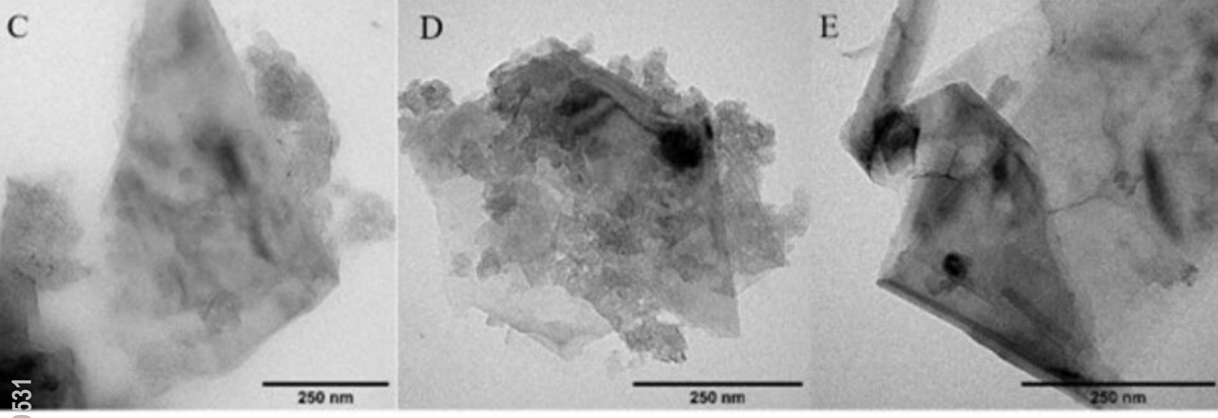


This is the author's peer reviewed, accepted manuscript. However, the online version of record will be different from this version once it has been copyedited and typeset.  
PLEASE CITE THIS ARTICLE AS DOI: 10.1122/8.0000531

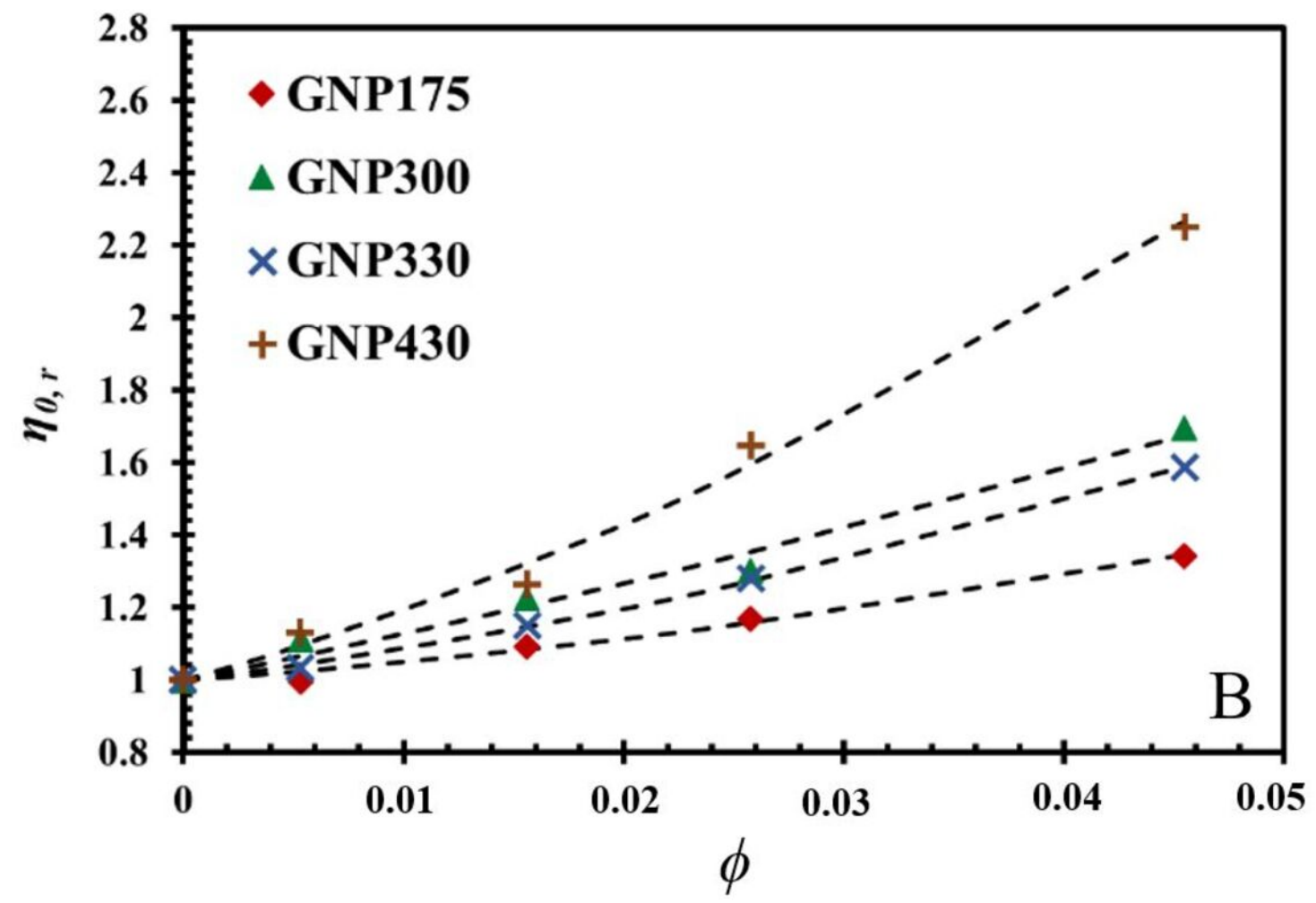
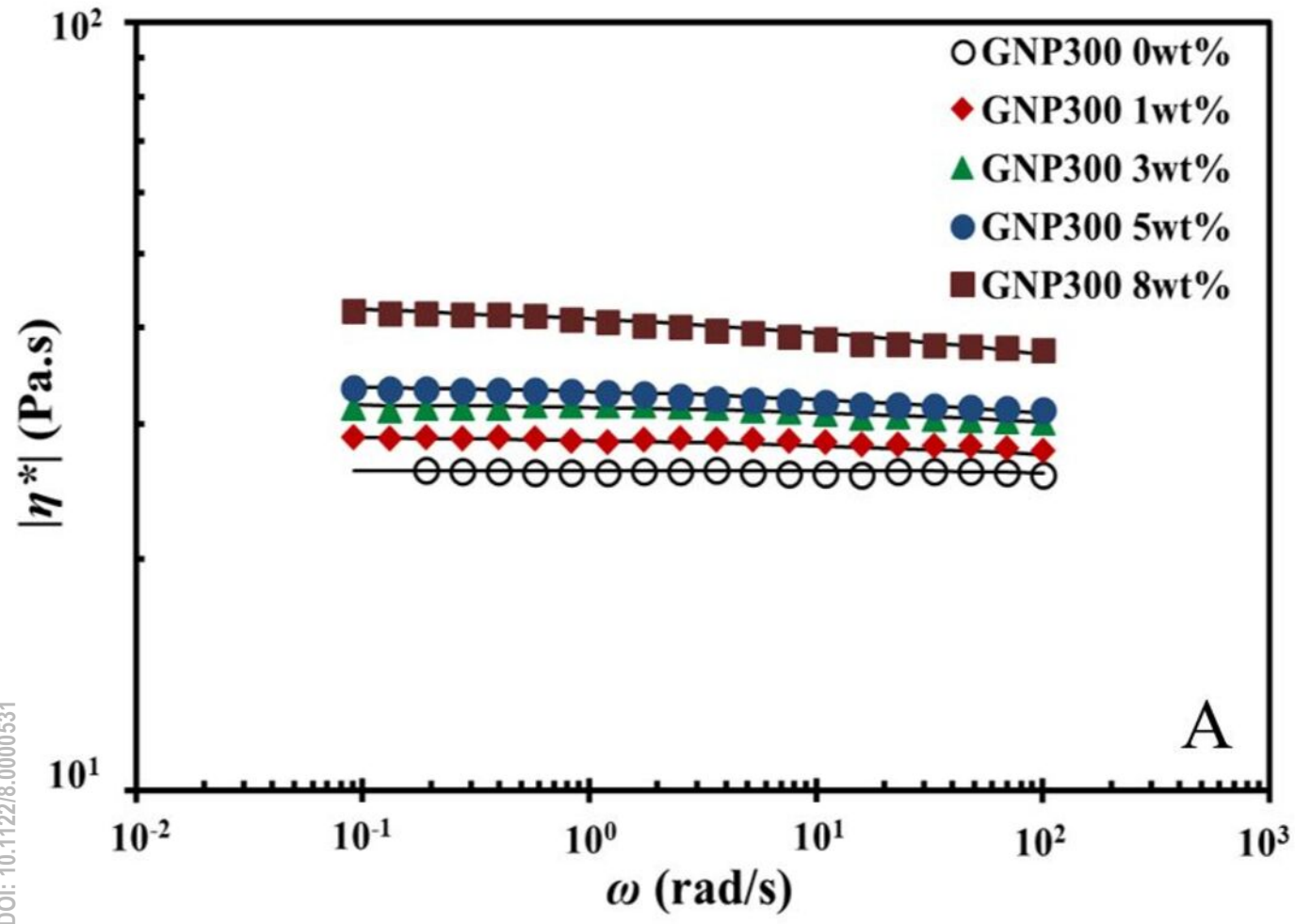


C

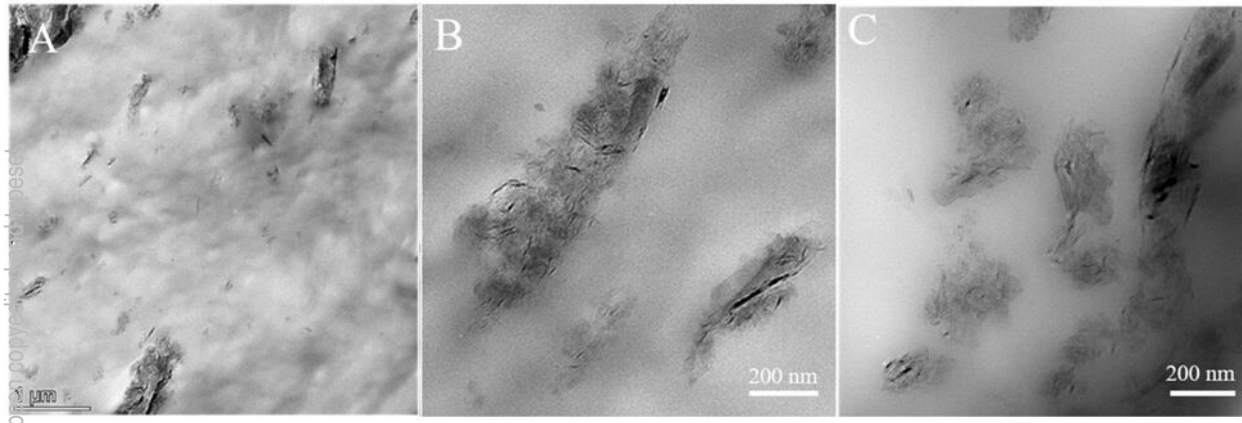
This is the author's peer reviewed, accepted manuscript. However, the online version of record will be different from this version once it has been copyedited and typeset.  
PLEASE CITE THIS ARTICLE AS DOI: 10.1122/1.5000031



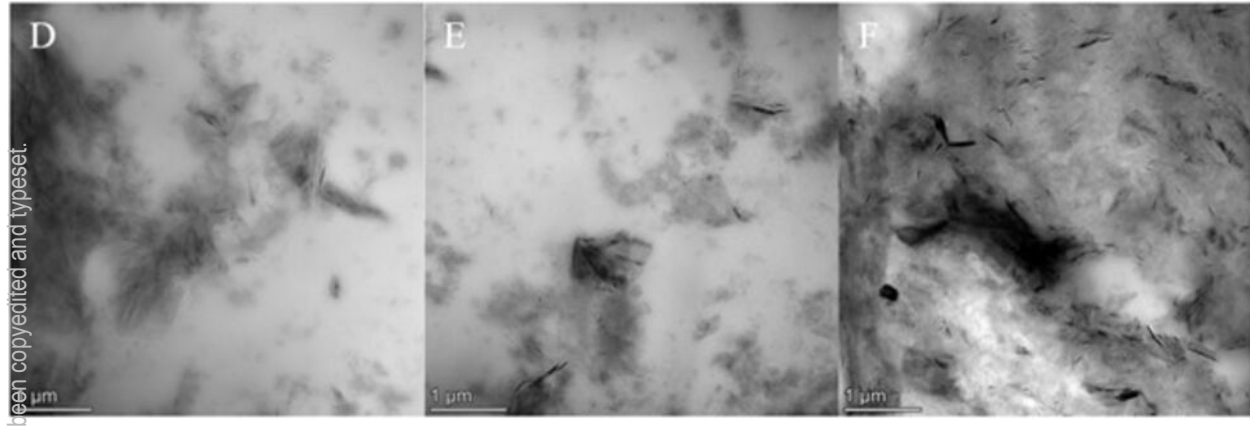
This is the author's peer reviewed, accepted manuscript. However, the online version of record will be different from this version once it has been copyedited and typeset.  
PLEASE CITE THIS ARTICLE AS DOI: 10.1122/1.5000053



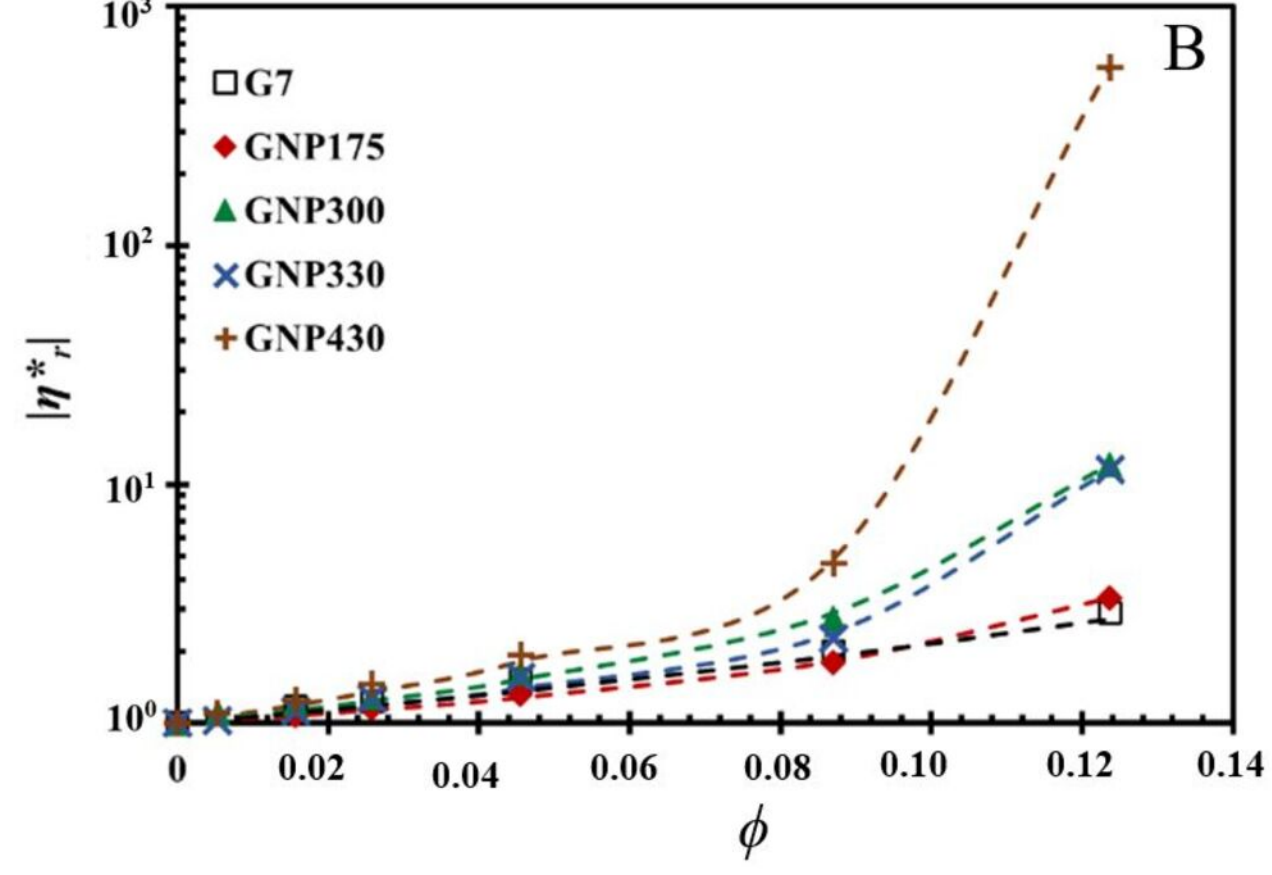
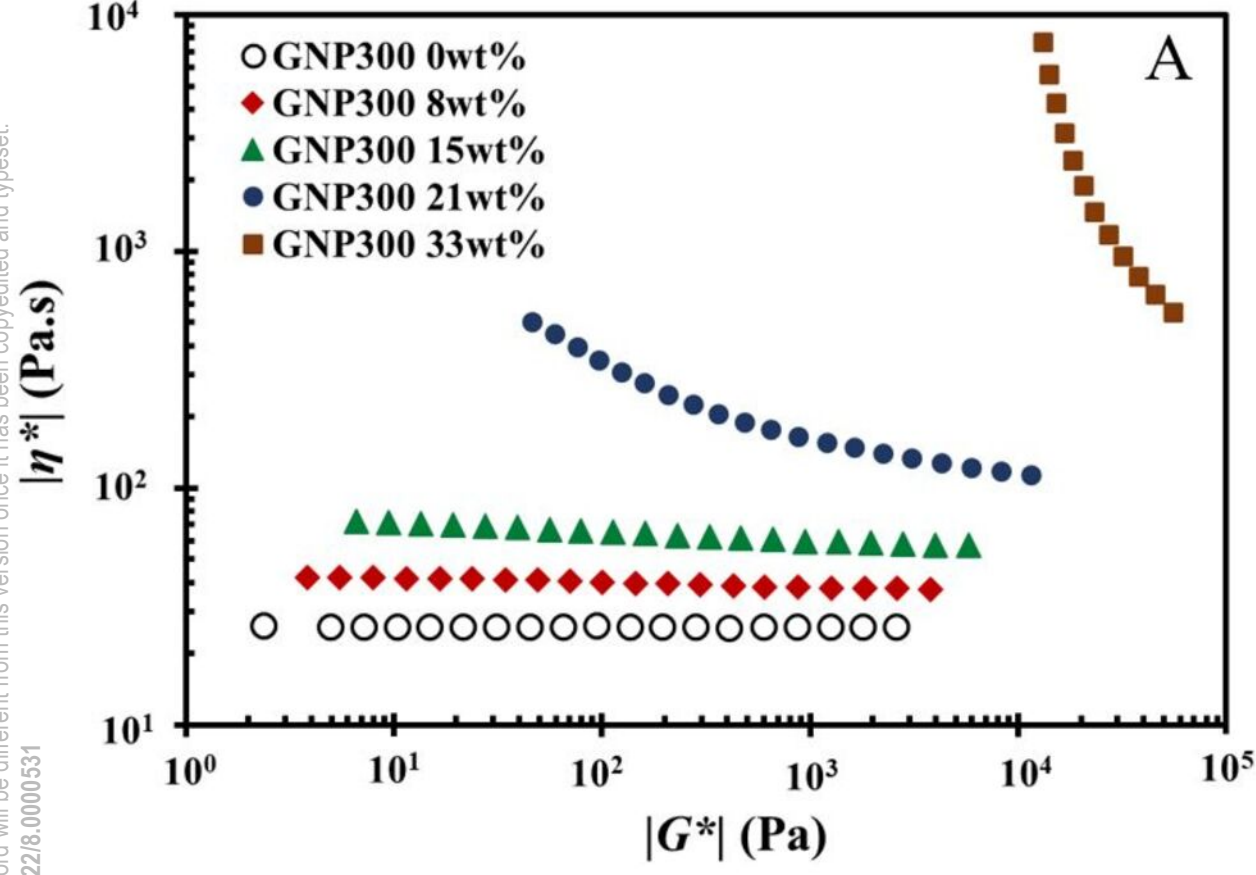
This is the author's peer reviewed, accepted manuscript. However, the online version of record will be different from this version once it has been copyedited and typeset.  
PLEASE CITE THIS ARTICLE AS DOI: 10.1122/1.50000531



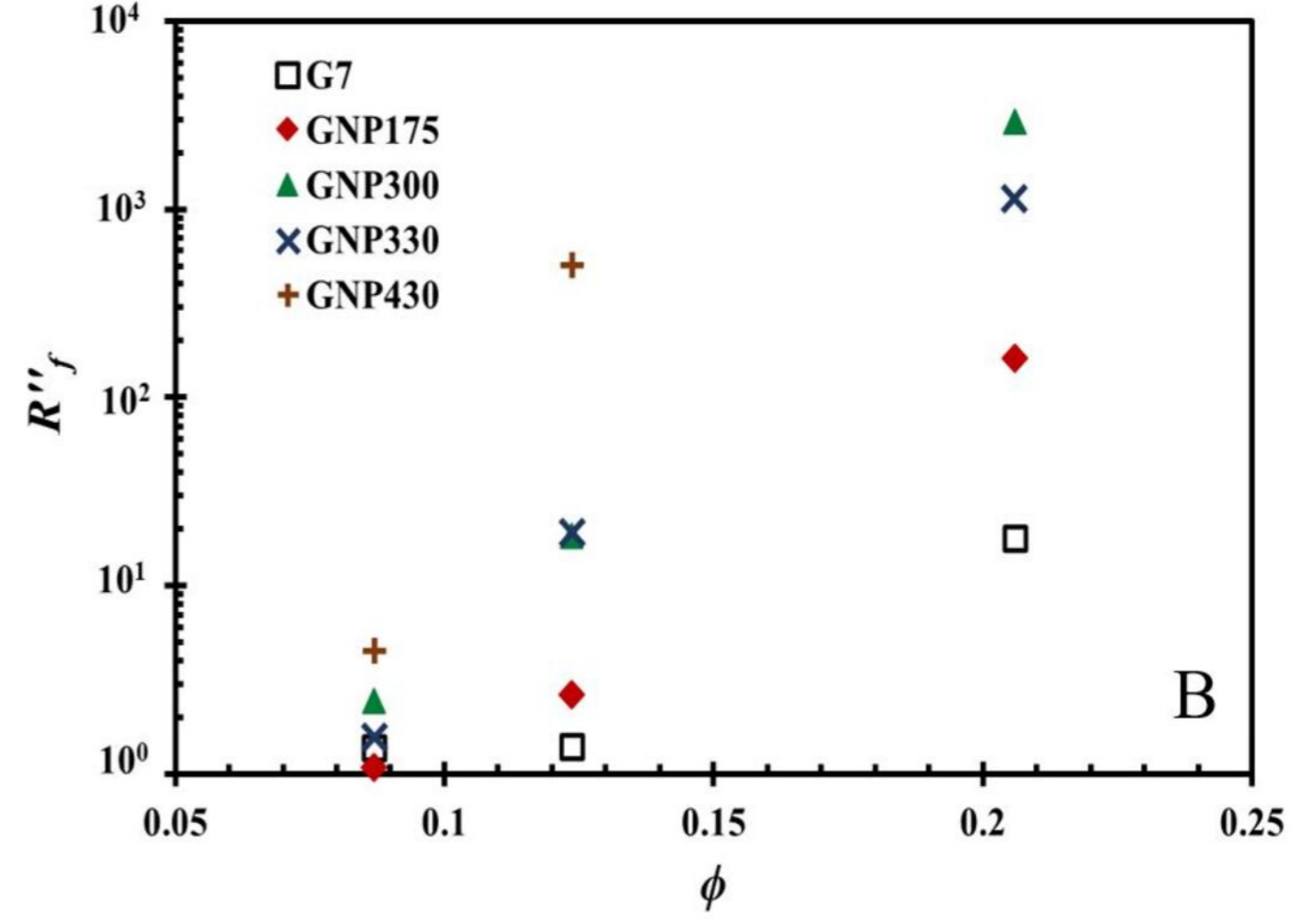
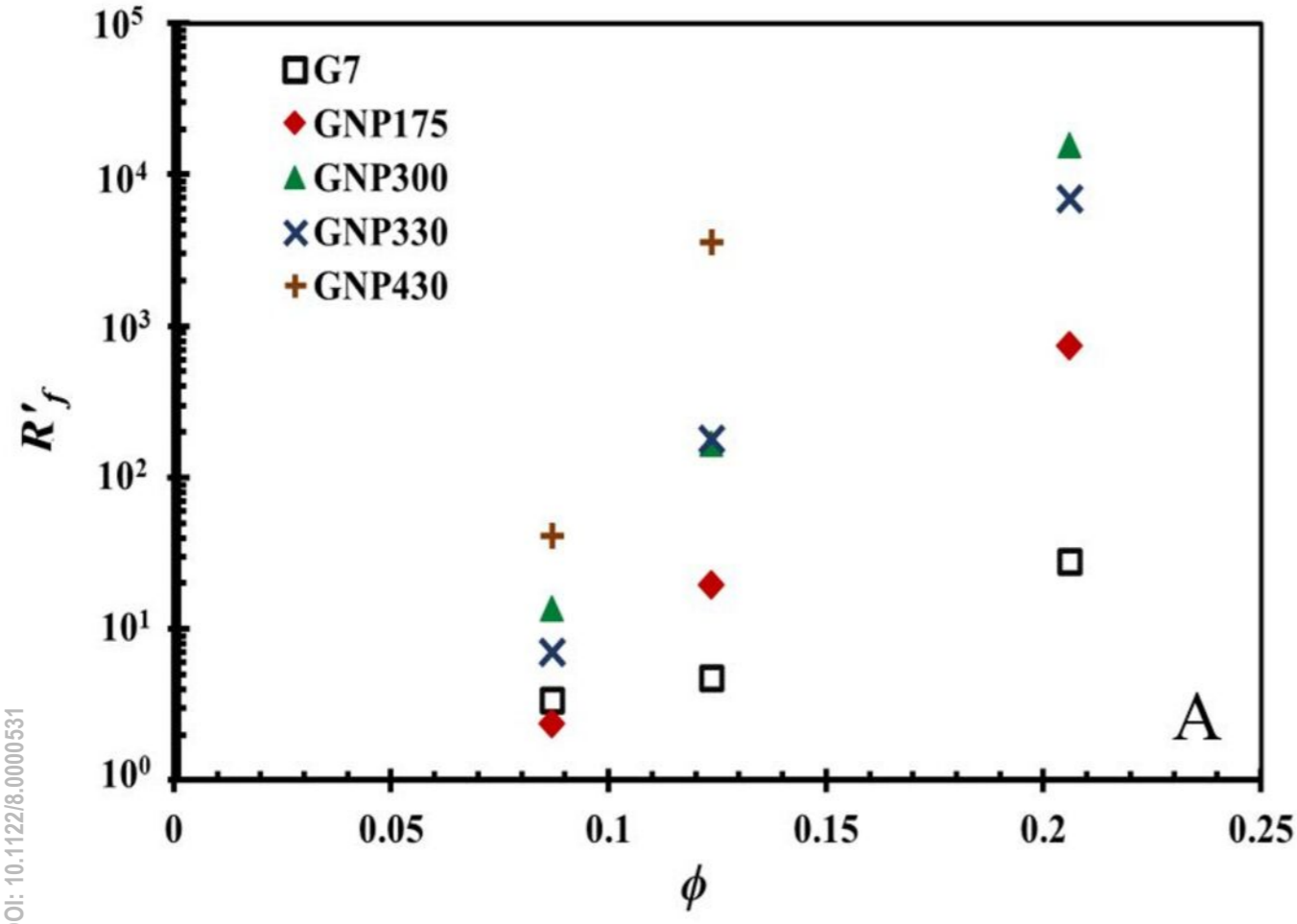
This is the author's peer reviewed, accepted manuscript. However, the online version of record will be different from this version once it has been copyedited and typeset.  
PLEASE CITE THIS ARTICLE AS DOI: 10.1122/8.0000531



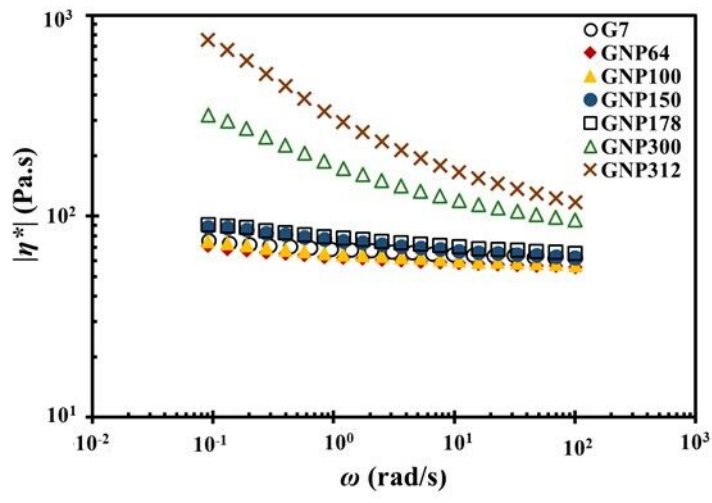
This is the author's peer reviewed, accepted manuscript. However, the online version of record will be different from this version once it has been copyedited and typeset.  
PLEASE CITE THIS ARTICLE AS DOI: 10.1122/8.0000531



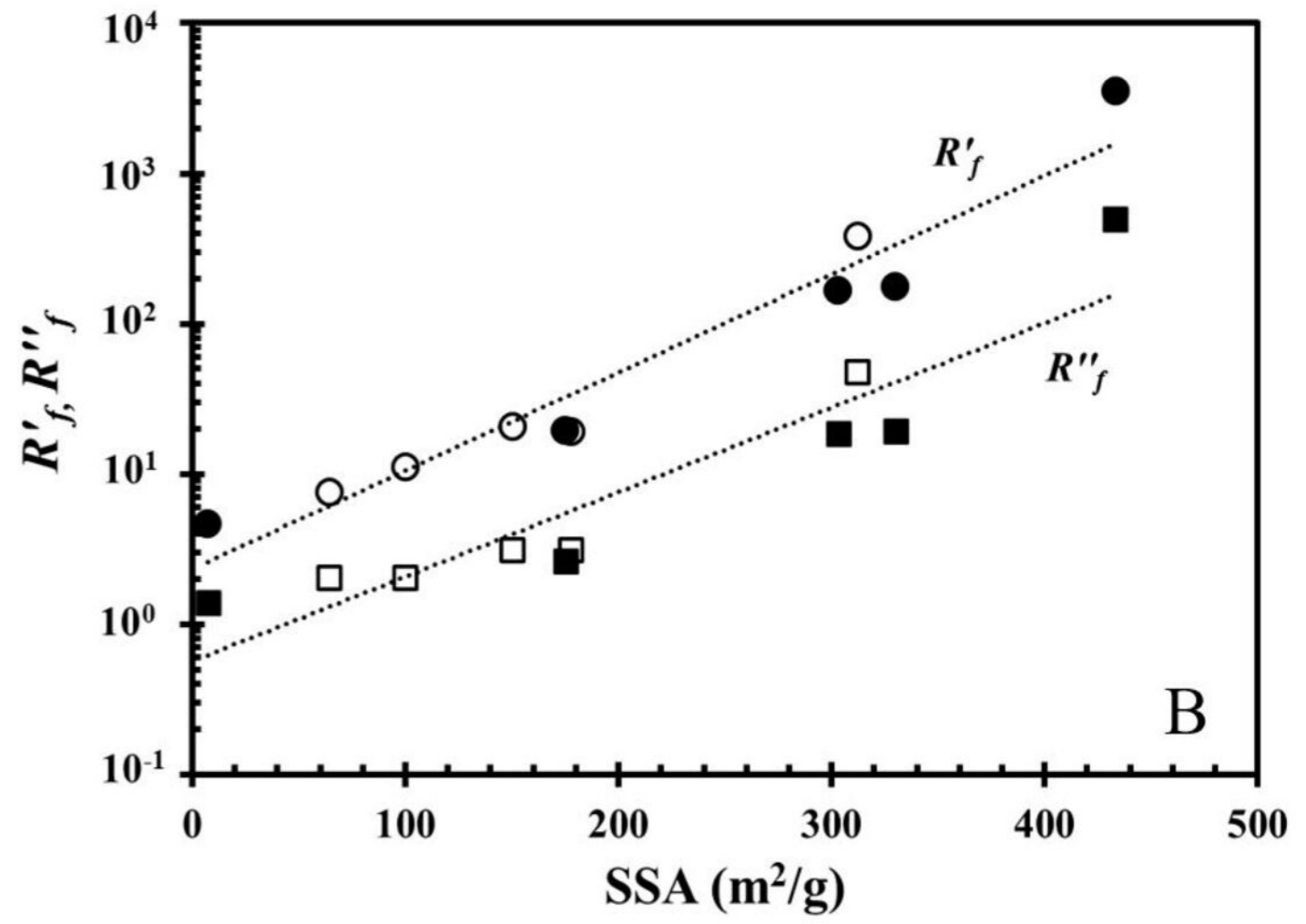
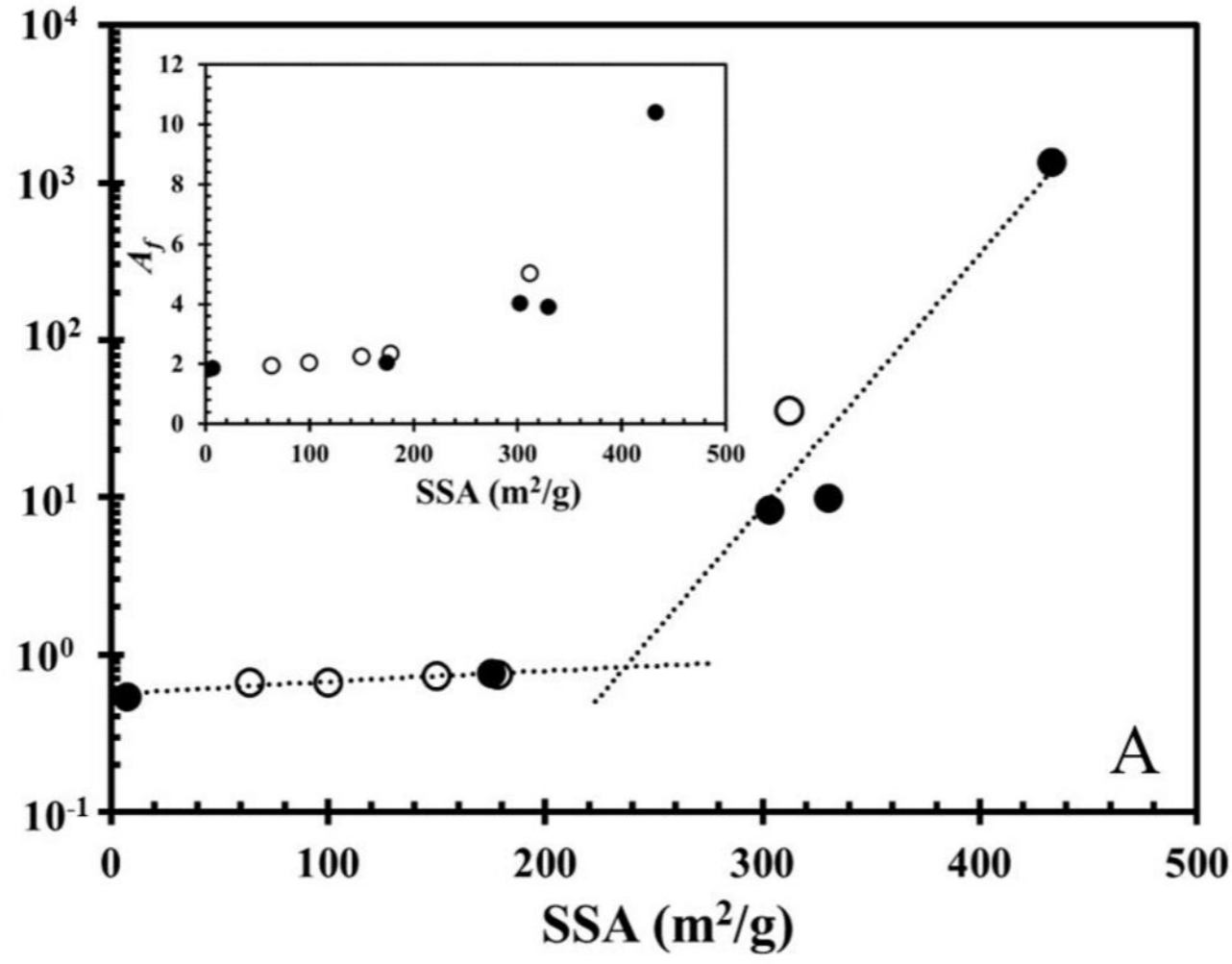
This is the author's peer reviewed, accepted manuscript. However, the online version of record will be different from this version once it has been copyedited and typeset.  
PLEASE CITE THIS ARTICLE AS DOI: 10.1122/1.8.0000531



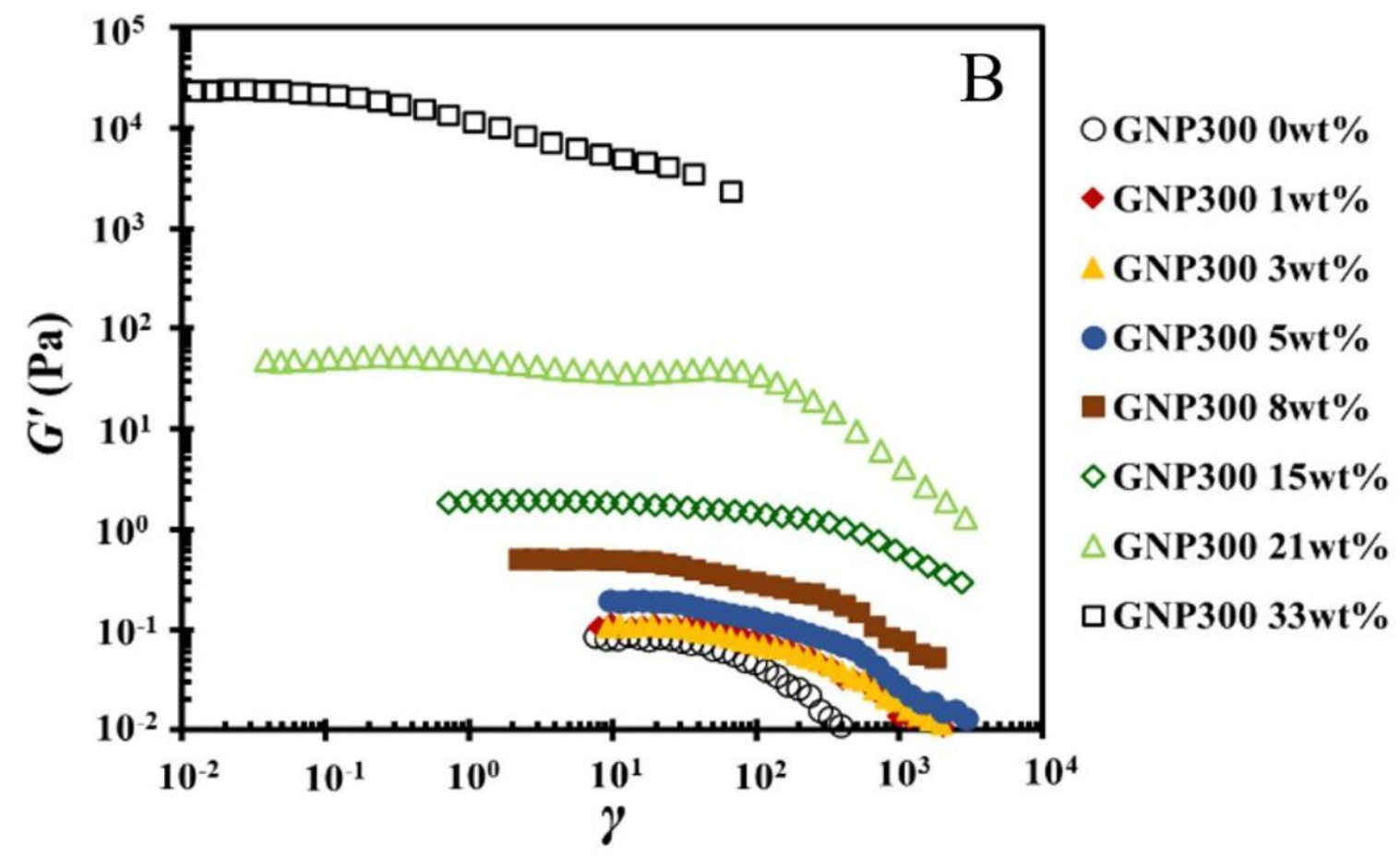
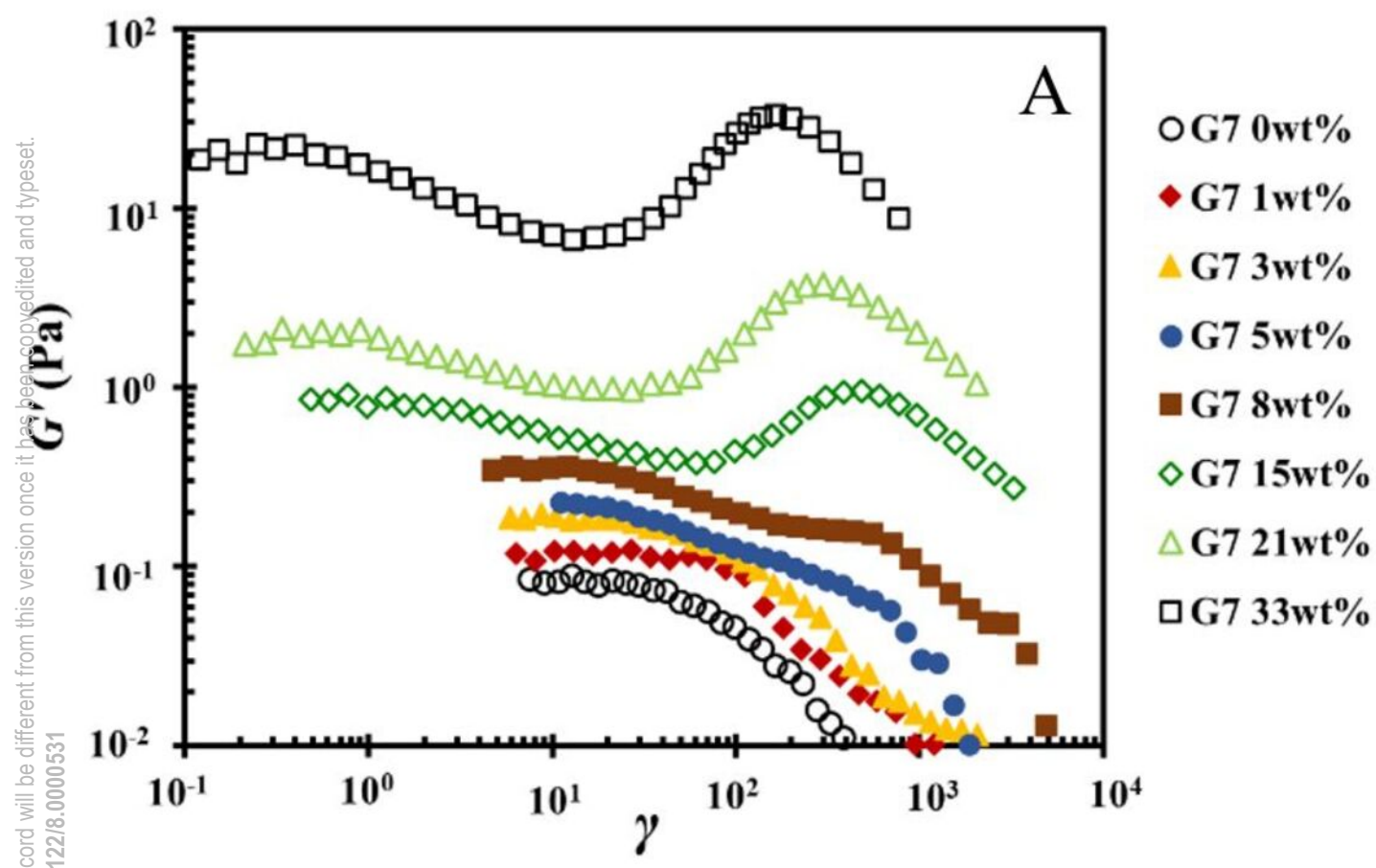
This is the author's peer reviewed, accepted manuscript. However, the online version of record will be different from this version once it has been copyedited and typeset.  
PLEASE CITE THIS ARTICLE AS DOI: 10.1122/8.0000531



This is the author's peer reviewed, accepted manuscript. However, the online version of record will be different from this version once it has been copyedited and typeset.  
PLEASE CITE THIS ARTICLE AS DOI: 10.1122/1.5000531



This is the author's peer reviewed, accepted manuscript. However, the online version of record will be different from this version once it has been copyedited and typeset.  
PLEASE CITE THIS ARTICLE AS DOI: 10.1122/1.5000531



This is the author's peer reviewed, accepted manuscript. However, the online version of record will be different from this version once it has been copyedited and typeset.  
 PLEASE CITE THIS ARTICLE AS DOI: 10.1122/8.0000531

